

Experimental dynamic characterization of friction brace dampers and application to the seismic retrofit of RC buildings

Panumas Saingam^{a,*}, Ryota Matsuzaki^b, Koki Nishikawa^a, Ben Sittler^a, Yuki Terazawa^a, Toru Takeuchi^a

^a Department of Architecture and Building Engineering, Tokyo Institute of Technology, Tokyo, Japan

^b Toda Corporation, Tokyo, Japan

ARTICLE INFO

Keywords:

Friction damper
Dynamic loading test
RC buildings
Seismic retrofit
Equivalent linearization

ABSTRACT

Previous earthquakes have caused extensive damage to reinforced concrete (RC) structures with insufficient lateral force resistance or energy dissipation capacity. There is a need to retrofit vulnerable existing RC buildings, particularly those not originally designed for seismic effects or designed to an outdated seismic specification. This study investigates the use of friction dampers as displacement-dependent energy dissipation devices to retrofit RC moment frame structures. First, an experimental program was conducted to characterize the dynamic behavior of friction brace dampers with several different materials, finding that a sintered metal compound provided a stable friction coefficient of 0.4. A strength-based equivalent linearization design procedure was then developed based on the required friction slip force and considering the cracked state of the existing RC structure. A four-story RC school building was then designed using the proposed retrofit design method, validated using nonlinear response history analysis and compared to a previous retrofit scheme that employed buckling-restrained braces (BRBs) and a stiffness-based equivalent linearization design method. The analysis results suggest that the proposed retrofit design method and friction brace dampers are effective in reducing the maximum story drift.

1. Introduction

Observations from previous earthquakes have often noted that older reinforced concrete (RC) buildings with insufficient lateral force resisting systems are susceptible to significant damage [1–6], yet these remain prevalent in countries with a newly recognized seismic hazard and limited tradition of seismic design. Unfortunately, this issue often extends to public buildings such as schools and hospitals, which play important post-disaster roles as shelters and in treating the sick and wounded. Public structures are typically assigned higher design forces by modern seismic design code with the intention of decreasing damage, ideally to a minimal level that permits immediate occupancy. Nevertheless, older RC buildings not originally designed for seismic loads or designed to an outdated seismic design code are vulnerable and require effective retrofit strategies.

Conventional retrofit of RC moment frames typically involves wrapping the RC columns with carbon fiber reinforced polymers [7,8], filling in bays with new RC shear walls [9,10] or adding conventional steel braces [11–14]. However, an alternative strategy is to increase the

energy dissipation by adding dampers, which have been shown to increase the seismic performance of new buildings [15–19], and to efficiently control the seismic response in retrofitted buildings. Dampers have also been proposed to retrofit RC buildings, most commonly using buckling-restrained braces (BRBs) to provide displacement-dependent energy dissipation [20–29]. Friction dampers (FD) offer a promising alternative, as they provide significant energy-dissipation from smaller story drifts [30–33] at a relatively low cost, and are easy to install and maintain [34]. Friction dampers may be employed as braces, in rocking walls, or at beam ends, such as the sliding hinge joints (SHJ) used in steel moment frames [35–37].

Friction brace dampers, in particular, affect the dynamic response by increasing stiffness and damping. Several studies have proposed displacement-based design methods for structures with energy dissipation devices [38–43], but these are typically iterative procedures, as the supplement damping depends on the resultant displacement. Displacement-based design has also been employed [44] to retrofit moment frames with in-plan irregularities, taking into account the strength and stiffness degradation from previous earthquakes. To avoid iteration, a direct equivalent linearization procedure was developed

* Corresponding author.

| Nomenclature | | | |
|-----------------|---|----------------------|---|
| A_{max} | Maximum roof acceleration | Q_{fc} | Lateral force at crack displacement |
| C_r | Damping reduction factor | Q_{fy} | Lateral force at yield displacement |
| d | Displacement amplitude | R | Damping response reduction factor |
| E_d | Hysteretic energy of the friction damper | S_{DS} | Design spectral acceleration at 0.2 sec |
| E_f | Hysteretic energy of the SDOF _{RC} | S_{D1} | Design spectral acceleration at 1.0 sec |
| $E_{\Sigma fe}$ | Total strain energy of the retrofitted SDOF | T_f | Fundamental period of the first vibration mode |
| f | Frequency | u_i | Fundamental modal displacement of i^{th} story |
| $F_{BRB,i}$ | Required yield strength of BRB at i^{th} story | V_{max} | Maximum slip velocity |
| $F_{BRBC,i}$ | Required yield strength of BRB at i^{th} story, reduced for partially composite steel frame | α_1 | Pre-yield stiffness ratio |
| F_d | Required lateral slip force of friction dampers | $\delta_{BRBy,i}$ | Lateral yield deformation of BRB at i^{th} story |
| $F_{d,i}$ | Required lateral slip force of friction dampers at i^{th} story | δ_{fc} | Lateral crack displacement |
| $F_{dc,i}$ | Required lateral slip force at i^{th} story, reduced for partially composite steel frame | δ_{fy} | Lateral yield deformation of the SDOF _{RC} |
| $\phi F_{d,i}$ | Axial slip force of individual friction brace damper | $\delta_{d,l}$ | Spectral displacement of the SDOF _{RC} model in the longitudinal direction |
| H_i | Height of i^{th} story | $\delta_{d,t}$ | Spectral displacement of the SDOF _{RC} model in the transverse direction |
| H_{eq} | Equivalent height of the SDOF _{RC} model | δ_{tar} | Lateral target displacement |
| $K_{BRB,i}$ | Required lateral BRB stiffness at i^{th} story | $\phi \delta_{dy,i}$ | Axial workpoint yield deformation of friction damper |
| $K_{BRBC,i}$ | Required lateral BRB stiffness at i^{th} story, reduced for partially composite steel frame | μ | Friction coefficient |
| $K_{f,i}$ | Story stiffness of existing RC building at i^{th} story, obtained by pushover analysis | $\bar{\mu}$ | Average friction coefficient |
| K_f | Lateral elastic stiffness of the SDOF _{RC} model | μ_c | Ratio of the crack-to-yield displacements (Ratio of δ_{fc} to δ_{fy}) |
| $K_{f,l}$ | Lateral stiffness of the SDOF _{RC} model in the longitudinal direction | μ_f | Drift ductility at the target roof displacement (Ratio of the δ_{tar} to δ_{fy}) |
| $K_{f,t}$ | Lateral stiffness of the SDOF _{RC} model in the transverse direction | λ | Unloading stiffness degradation parameter |
| $K_{f\mu}$ | Secant stiffness of the SDOF _{RC} | ξ_{f0} | Intrinsic damping of the existing RC frame |
| $\phi K_{d,i}$ | Axial workpoint stiffness of individual friction brace damper | ξ_{eq} | Average equivalent hysteretic damping ratio of the retrofit structure |
| $K_{RC,i}$ | Lateral stiffness of RC frame at the i^{th} story within the retrofit bay | ξ'_{eq} | Equivalent hysteretic damping ratio of the retrofit structure |
| $K_{SF,i}$ | Lateral stiffness of steel frame at the i^{th} story | $\xi_{f\mu}$ | Equivalent hysteretic damping of SDOF _{RC} |
| m_i | Mass of i^{th} story | θ_{dy} | Yield story drift of friction damper for brace design |
| M_{eq} | Equivalent mass of the SDOF _{RC} model | $\theta_{f\mu}$ | Story drift of the SDOF _{RC} model |
| N_{b1} | Friction load cell 1 | θ_{max} | Maximum story drift |
| N_{b2} | Friction load cell 2 | θ_{tar} | Target story drift |
| p | Stiffness reduction factor | $\theta_{tar,i}$ | Target story drift of i^{th} story |
| Q_i | Lateral force distribution along the building height for the i^{th} story | $\gamma_{cf,i}$ | Fully composite stiffness amplification ratio at i^{th} story, expressing the fully composite stiffness relative to the non-composite stiffness of the RC and steel frames |
| | | $\gamma_{cp,i}$ | Partially composite stiffness amplification ratio at i^{th} story, expressing the actual composite stiffness obtained from pushover analysis relative to the non-composite stiffness of the RC and steel frames |

[45] for the seismic design of passively controlled steel structures based on the damper stiffness. This method has since been applied to RC buildings retrofitted with BRBs and elastic steel frames [27,28] and is referred to as the constant drift (CD) method in this paper, as it targets a constant inelastic story drift. This study expands the CD method to RC buildings retrofitted with friction brace dampers.

Before investigating the design method and application, this study first presents an experimental program characterizing the dynamic behavior of the proposed friction damper. Five different friction materials were investigated to identify an optimal material exhibiting a high, stable friction coefficient with minimal dependencies. The stiffness-based CD method is then extended to a strength-based method, which is more appropriate for friction dampers where the salient parameter is the required slip force, instead of the brace stiffness. Installing new braces into an existing RC frame often requires supplemental steel frames, and a previous study [46] found that the partial composite behavior between the existing RC and new steel frame may reduce the required damper. In this study, the composite behavior is used to reduce the friction damper's slip force demand. Finally, a simple design recommendation is outlined, and applied to a design example of a four-

story RC school in Thailand. The effectiveness of the proposed friction damper retrofit and design method is demonstrated and validated using nonlinear response history analysis.

2. Friction damper experiment

Previous studies have tested friction dampers, but have either achieved a high, but unstable friction coefficient or a moderate, but stable friction coefficient. Metallic asymmetric friction dampers [47] (including aluminum shims, brass shims, steel shims, bisalloy 80, bisalloy 400, and bisalloy 500) have achieved initial friction coefficients of up to 0.48, but reported values as low as 0.30 for large-amplitude dynamic loading. Conversely, a friction damper widely used in practice [48] produces a stable, but slightly lower friction coefficient of 0.31. This study sought to develop a friction damper that exhibits a high and stable friction coefficient, decreasing the required normal force while increasing the device reliability. An experiment was conducted to obtain the dynamic friction coefficient and dependencies of several different friction materials.

Five automotive brake pad materials were considered: Polymer

Table 1
Definition of experimental specimens.

| Specimen name | Component of material |
|-----------------------|---|
| Polymer composite A-1 | Polymer composite (non-asbestos, non-steel) with abrasive particles and fibers cast in organic resin (4B06*) |
| Polymer composite A-2 | Polymer composite with abrasive particles and fibers cast in organic resin, with a lower ratio of abrasive contents than Polymer composite A-1, adding lubrication contents (TD26*) |
| Polymer composite B | Polymer composite with abrasive particles and fibers cast in organic resin, with a lower ratio of abrasive contents than Polymer composite A-1 (TD08*) |
| Sintered metal C-1 | Sintered metal with abrasive particles (H3K*) |
| Sintered metal C-2 | Sintered metal with abrasive particles with a lower ratio of abrasive contents than Sintered metal C-1 (H3KJA*) |

* Material code from Showa Denko Materials Co. Ltd.

composite A-1, Polymer composite A-2, Polymer composite B, Sintered metal C-1, and Sintered metal C-2. The polymer composites included abrasive particles and non-steel fibers (aramid, copper, etc.) cast in organic resin. Polymer composite B featured a lower ratio of the abrasive particles than A-1, while A-2 also featured a lower ratio and was infused with a lubricant. The sintered metal materials were fabricated using several metal powders, while C-1 featured a higher ratio of abrasive particles than C-2. The five materials are summarized in Table 1.

2.1. Test specimens

A representative friction damper specimen is shown in Fig. 1. The test rig was reused from previous friction tests [48–50]. Each specimen was composed of a stainless-steel sliding plate with 65 mm holes (Fig. 1a) and two 4.5 mm steel outer plates (Fig. 1b), which were welded to the actuator assembly and bonded to the friction material (Fig. 1c). The sliding plate was sandwiched between the two outer plate assemblies, and fixed using grade 10.9 M27 bolts, each with five cone disc springs (outer diameter 100 mm, inner diameter 51 mm, thickness 6 mm). The bolts were tightened to a normal force of 166 kN, producing an average surface pressure at the friction interface of about 9.7 MPa.

2.2. Test setup and loading protocol

The experimental setup is depicted in Fig. 2a and 2b. The friction damper specimens were loaded by applying horizontal displacement to the shake table and sliding plate. The reaction force was measured by a load cell attached to the reaction beam and outer plate assembly, while the relative slip displacement was measured using lasers attached to the bolts. Finally, the axial force in the bolts was confirmed using individual load cells (N_{b1} , N_{b2}), as indicated in Fig. 1.

The loading protocols were developed to systematically investigate the friction dependencies, and the frequencies and displacement amplitudes satisfied the damper test criteria of ASCE 7-16 Chapter 18 [51]

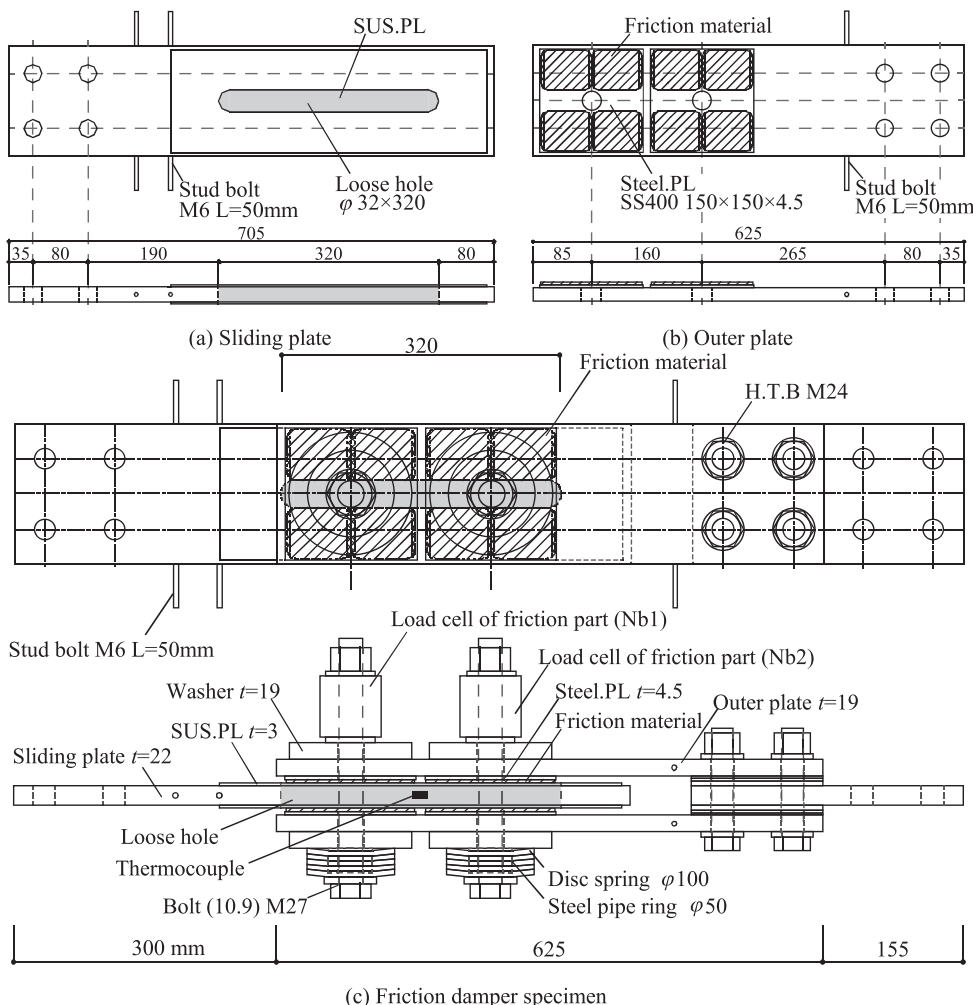


Fig. 1. Friction damper specimen.

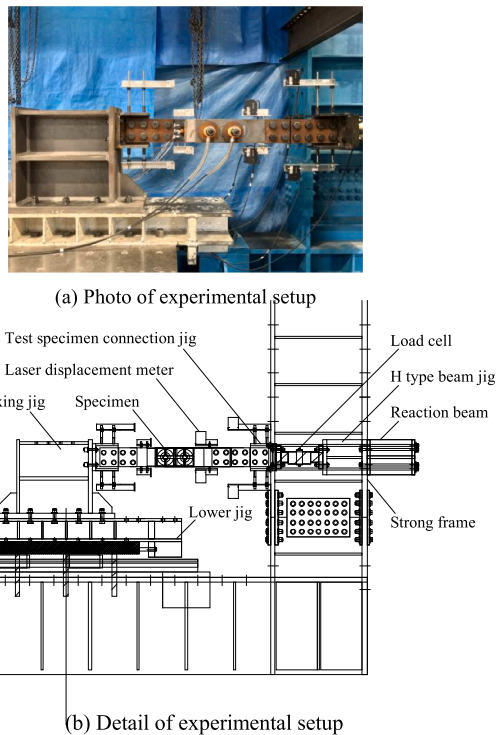


Fig. 2. Experimental setup.

for typical mid-to-high rise buildings with fundamental periods exceeding $T > 0.7$ sec. Table 2 summarizes the adopted loading protocols, including the displacement amplitude, frequency, waveform and number of cycles per set. The loading rate varied from quasi-static to dynamic, and the displacement amplitude from ± 20 to 55 mm. The full loading protocol specified in Table 2 was applied to each of the five specimens.

2.3. Experimental results

2.3.1. Friction hysteresis

Representative slip force and friction coefficients are shown in Fig. 3a to 3e for each material (Set No. 9: 4 cycles at ± 40 mm and 0.7 Hz). The normalized shear forces were obtained by dividing the horizontal reaction force by the total normal force and number of slip planes. The polymer composite materials generated slightly higher friction coefficients than the sintered metal materials, but the rigid-plastic hysteresis was more stable for the sintered metal materials.

Fig. 3a indicates that the polymer composite material A-1 had a slip load of 300 kN, which corresponds to a friction coefficient of 0.50, the highest value of all the materials. Although the polymer composite material B (Fig. 3c) exhibited a similar maximum slip force and friction coefficient as A-1, the friction coefficient was less stable and experienced

stick-slip behavior, with frequent sudden small drops in force. Conversely, the materials A-2 and C-1 exhibited a slip force of about 250 kN, which corresponds to a friction coefficient of 0.45, as indicated by Fig. 3b and 3d, respectively. In addition, Fig. 3e presents a slightly lower friction coefficient of material C-2 than A-2 and C-1. These materials also featured a more stable rigid-plastic hysteresis than materials A-1 and B.

2.3.2. Cyclic variation of friction coefficient during continuous loading

The slip force-relative displacement, friction coefficient-relative displacement, and axial bolt force (i.e., normal force) are shown in Fig. 4a to 4e for the 100-cycle continuous loading (Set No.18), and the evolution in the friction coefficient in Fig. 5. These figures indicate that the sintered metal materials (C-1 and C-2) exhibited less fluctuation in the friction coefficients than the polymer composite materials (A-1, A-2, and B). For example, while the friction coefficient of the polymer composite materials ranged from 0.30 to 0.50, the sintered metal materials only varied from 0.40 to 0.50.

The increase in temperature due to cycle heating during continuous loading is shown in Fig. 6, which occurs as the friction dissipates energy through heat. Note that the specimens were cooled to 45 °C between each set.

2.3.3. Wear of friction material surface at end of testing

The friction material surfaces are shown in Fig. 7 at the end of each test. The polymer composite materials A-1 (Fig. 7a) and A-2 (Fig. 7b) were significantly darkened, while evidence of melting was also observed due to high temperatures developed in the final set. The polymer composite material B (Fig. 7c) was also darkened, but melting was not observed. All three of these polymer composite materials experienced greater wear closer to the bolt holes, which indicates that the friction damper did not apply a perfectly uniform pressure. Conversely, the sintered metal materials C-1 and C-2 exhibited relatively uniform wear, as shown in Fig. 7d and 7e.

2.4. Friction coefficient dependencies

The friction coefficient dependencies were developed from the dynamic test results, with the average friction coefficient ($\bar{\mu}$) calculated from the hysteretic energy and slip for each cycle (Fig. 8), and then averaged across the full set.

2.4.1. Cyclic loading dependence

The average friction coefficients for each set are shown in Fig. 9. These varied significantly for the polymer composite material B (Fig. 9c), but by less than $\pm 10\%$ for the polymer composite materials A-1 (Fig. 9a) and A-2 (Fig. 9b), and were essentially constant for the sintered metal materials C-1 (Fig. 9d) and C-2 (Fig. 9e). The cyclic heating during the final 100 cycle sets generally produced the greatest deviation and lowest friction coefficients for the polymer composite materials, but had negligible effect on the sintered metal materials.

2.4.2. Displacement amplitude dependence

The displacement amplitude dependence is shown in Fig. 10a to 10e for the friction materials A-1, A-2, B, C-1, and C-2, respectively. The

Table 2
Loading protocol.

| Set No. | Amplitude (mm) | Frequency (Hz) | Input waveform | Cycles |
|-----------------|----------------|-----------------------------------|-----------------|--------|
| 1 (Standard) | ± 50 | Quasi static (0.01) | Sine wave | 2 |
| 2-5 | ± 20 | Dynamic (0.3, 0.5, 0.7, 1.0) | Sine wave | 4 |
| 6-10 | ± 40 | Dynamic(0.05, 0.3, 0.5, 0.7, 1.0) | Sine wave | 4 |
| 11-14 | ± 55 | Dynamic (0.05, 0.3, 0.5, 0.7) | | |
| 15-16 | $\pm 20, 40$ | Dynamic (0.7) | Triangular wave | |
| 17 (Standard) | ± 50 | Quasi static (0.01) | Sine wave | 2 |
| 18 (Continuous) | ± 20 | Quasi static (0.5) | Sine wave | 100 |

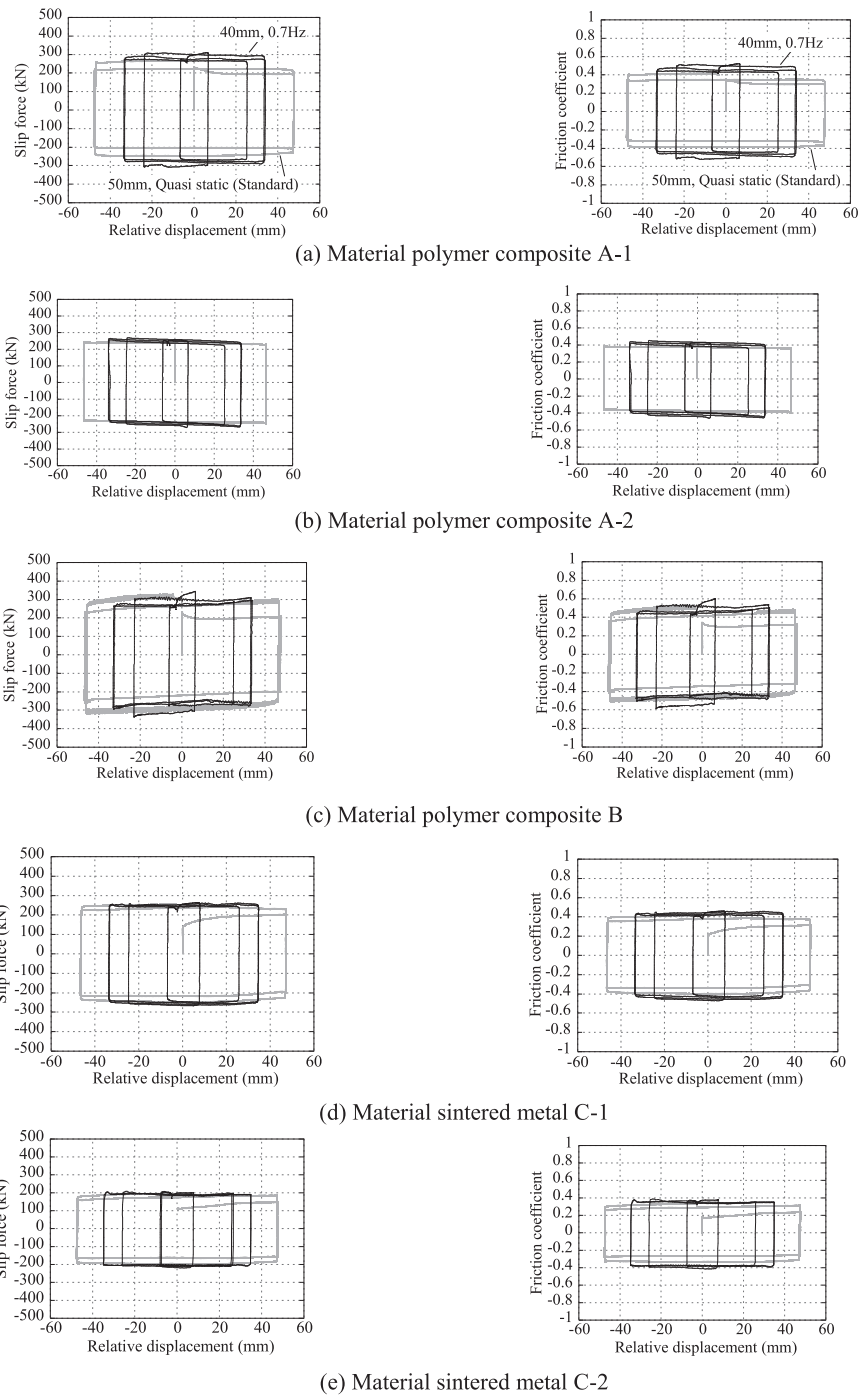


Fig. 3. Results of dynamic loading tests (± 50 mm, Quasi-static; ± 40 mm, 0.7 Hz).

polymer composite material B exhibited the greatest variation, particularly at the larger 40 and 55 mm amplitudes. The polymer composite materials A-1 exhibited friction coefficients that gradually increased from 0.42 to 0.58 between the amplitudes 20 and 55 mm. Conversely, the polymer composite material A-2, sintered metal materials C-1 and C-2 exhibited negligible amplitude dependence, which remained stable at 0.40 over the amplitude range from 20 to 55 mm.

2.4.3. Slip velocity dependence

The slip velocity dependence is shown in Fig. 11a to 11e for the friction materials A-1, A-2, B, C-1, and C-2, respectively. For the sets with sinusoidal input motion, the maximum slip velocity (V_{max}) was

derived from the amplitude (d) and the frequency (f) following Equation 1.

$$V_{max} = 2\pi df \tag{1}$$

The polymer composite material A-1 exhibited larger friction coefficients at lower velocities between the amplitudes 40 and 55 mm, while the polymer composite material A-2 exhibited smaller friction coefficients at lower velocities between the amplitudes 20 and 40 mm. Nevertheless, the velocity dependency was negligible for V_{max} exceeding 100 mm/sec for both materials. Up to a 50% reduction in the friction coefficient was observed for the polymer composite material B between the quasi-static and maximum velocity ($V_{max} = 250$ mm/sec). Once

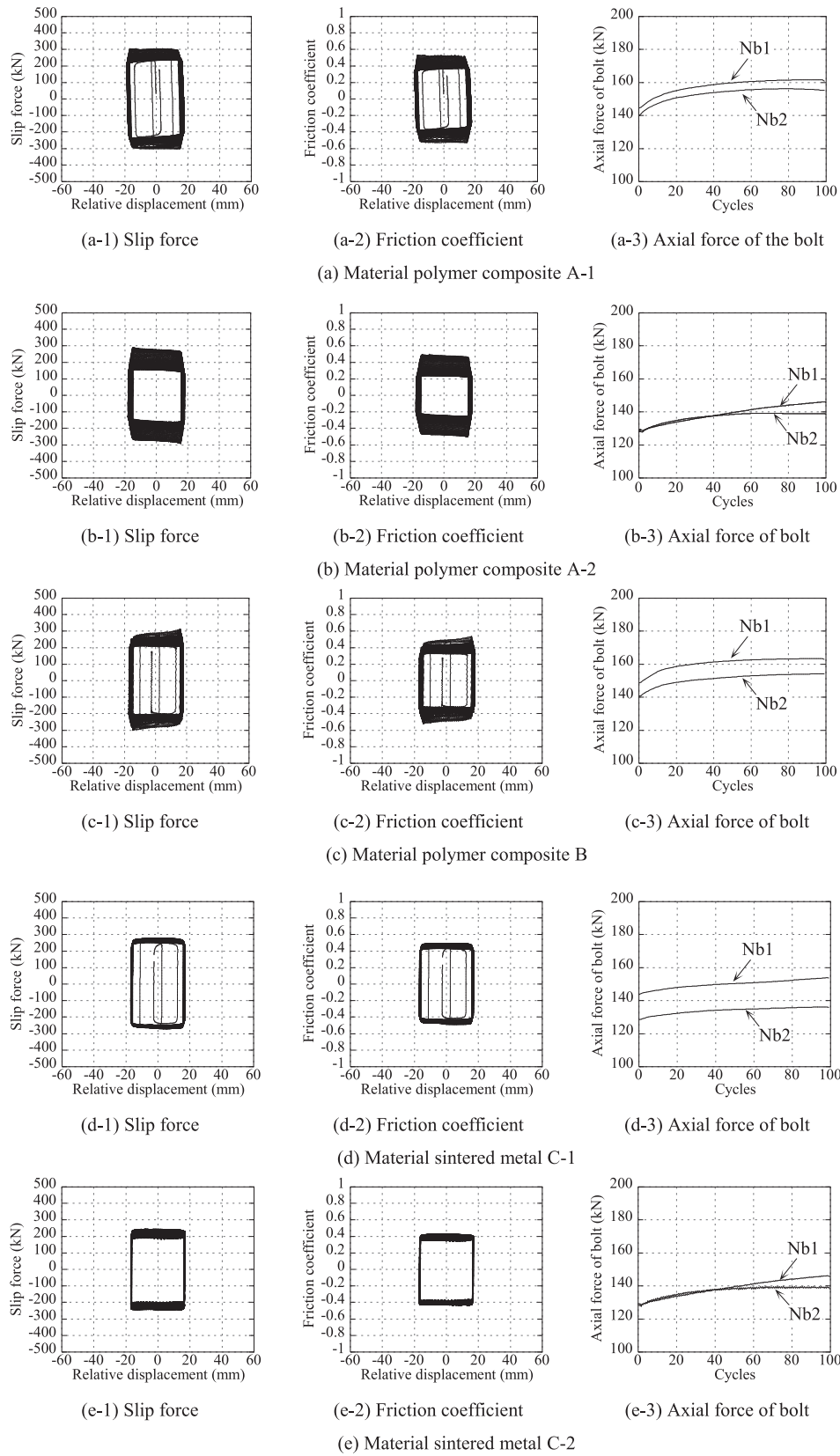
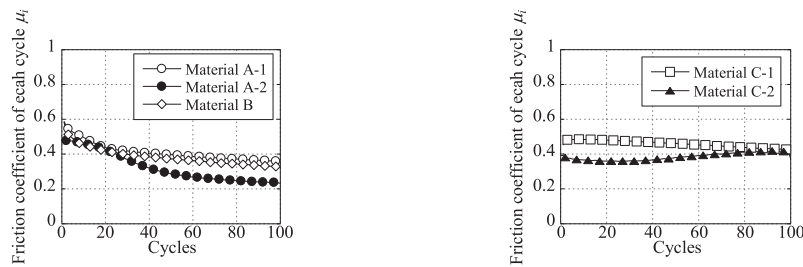
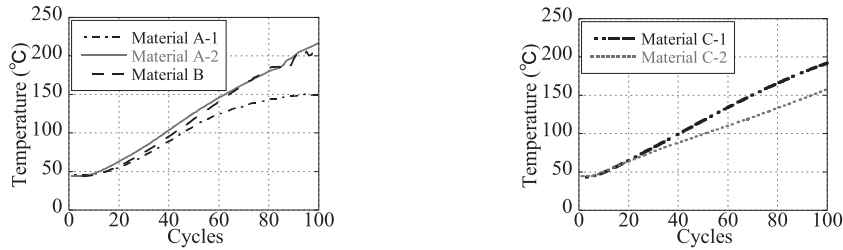


Fig. 4. Results of continuous loading tests (± 20 mm, 0.5 Hz).



(a) Polymer composite materials (A-1, A-2 and B) (b) Sintered metal materials (C-1 and C-2)

Fig. 5. Friction coefficient-cycles.



(a) Polymer composite materials (A-1, A-2 and B) (b) Sintered metal materials (C-1 and C-2)

Fig. 6. Temperature cycles.

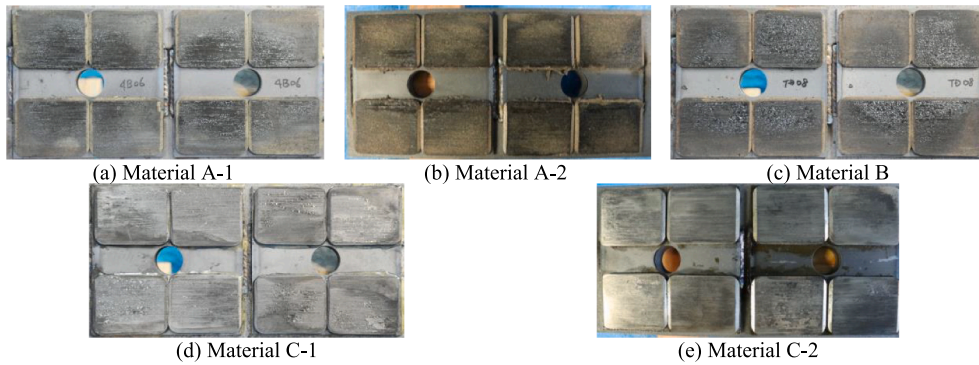


Fig. 7. Friction material surfaces at end of test.

again, the sintered metal materials C-1 and C-2 exhibited negligible velocity dependence and remained stable at 0.40 over the amplitude range from 20 to 55 mm.

2.4.4. Temperature dependence

The temperature dependence is shown in Fig. 12a, 12b, and 12c for the friction materials A-1, B, and C-1, respectively. The friction coefficient gradually decreased for the polymer composite materials A-1 and B due to the cumulative cyclic heating, but remained stable for the sintered metal material C-1, even for temperatures reaching 200 °C.

2.5. Summary of experiment

The friction experiment identified the dynamic friction characteristics of several candidate friction brace damper materials. Of these, the sintered metal material C-1 exhibited the most stable friction coefficient at $\bar{\mu} = 0.40$, with negligible amplitude, velocity and temperature dependencies. Therefore, this material was selected for the seismic retrofit design study, while the lack of friction coefficient dependencies permits it to be modelled using a perfectly elasto-plastic hysteresis (i.e., Coulomb friction model).

3. Retrofit design method

This section introduces a seismic design method to retrofit RC buildings with friction brace dampers. The proposed procedure involves obtaining the single degree of freedom (SDOF) properties of the existing RC building, calculating the required damper slip force and then vertically distributing the friction dampers. A preferred installation method is to attach the dampers to inscribed single-bay steel frames (SF), in which case partial composite behavior develops between the RC and steel frames.

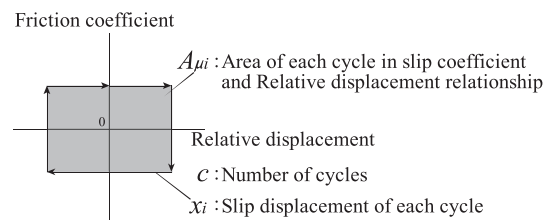


Fig. 8. Calculation of average friction coefficient.

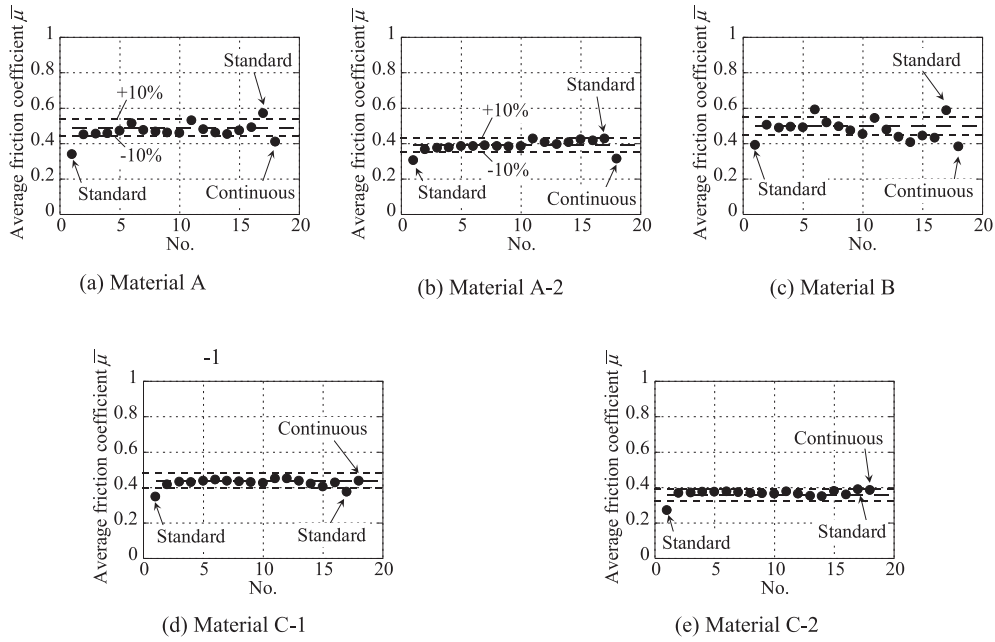


Fig. 9. Cyclic variation of average friction coefficient.

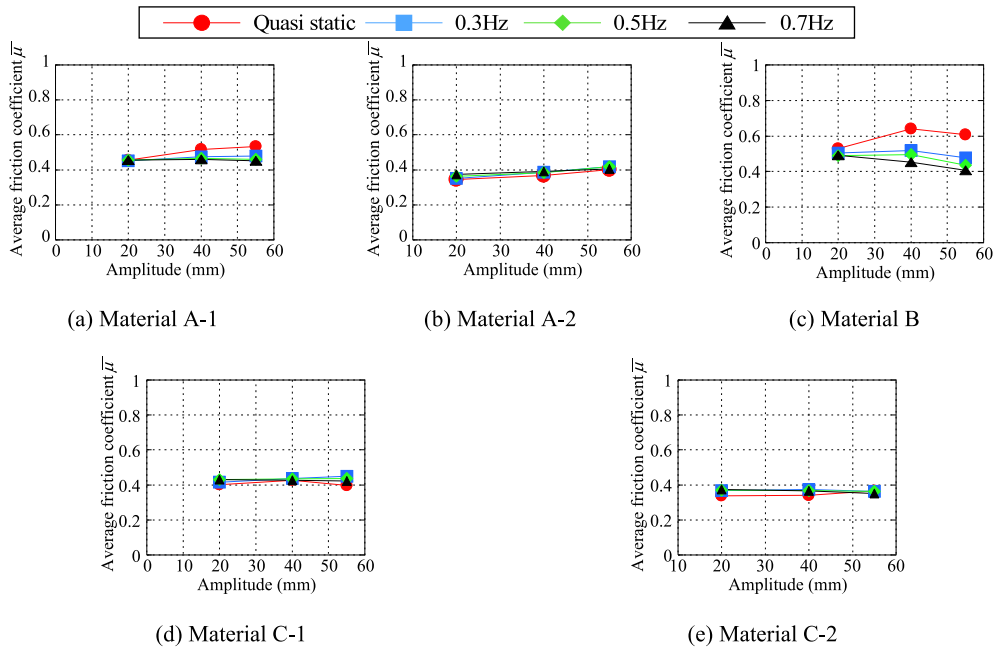


Fig. 10. Average friction coefficient - amplitude relationship.

3.1. Simplification of RC building to single degree of freedom

First, the existing RC frame is simplified into a single degree of freedom (SDOF_{RC}) model (Fig. 13) following a well-known concept [52,53] employed in previous studies [23,27,54]. The equivalent height H_{eq} (Equation 2), equivalent mass M_{eq} (Equation 3), and elastic lateral stiffness K_f (Equation 4) may be calculated from the mass m_i , fundamental modal displacement u_i and height H_i for each story i^{th} , and the elastic fundamental period T_f [23,53,54].

$$H_{eq} = \frac{\sum_{i=1}^N m_i \cdot u_i \cdot H_i}{\sum_{i=1}^N m_i \cdot u_i} \quad (2)$$

$$M_{eq} = \frac{(\sum_{i=1}^N m_i \cdot u_i)^2}{\sum_{i=1}^N m_i \cdot u_i^2} \quad (3)$$

$$K_f = \left(\frac{2\pi}{T_f}\right)^2 M_{eq} \quad (4)$$

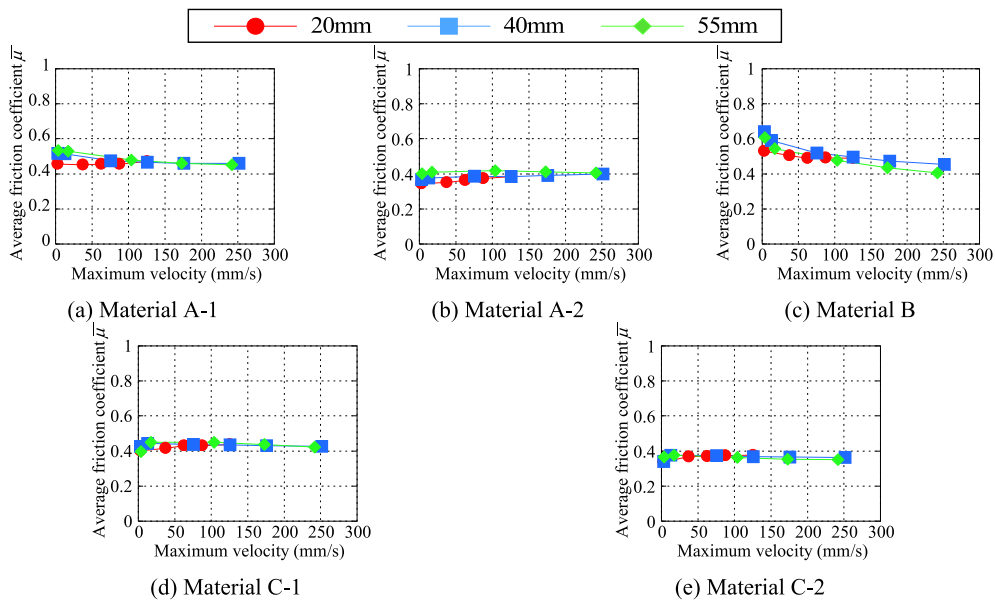


Fig. 11. Average friction coefficient - maximum velocity relationship.

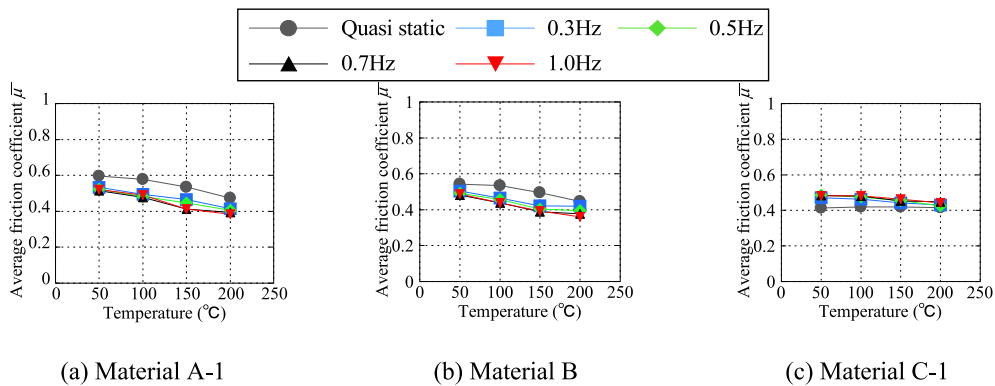


Fig. 12. Average friction coefficient temperature relationship.

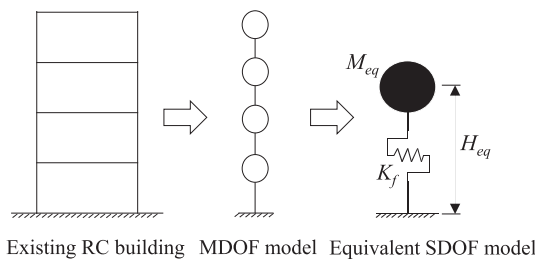


Fig. 13. Simplification of the RC building to SDOF model.

Next, the base shear-roof displacement relationship of the RC frame is obtained using nonlinear modal pushover analysis (based on the fundamental mode) in order to estimate the cracking (δ_{fc}) and yielding (δ_{fy}) roof drift displacements and corresponding base shear forces (Q_{fc} , Q_{fy}). It is also useful to obtain the story strengths ($Q_{fy,i}$), as these are used later to vertically distribute the dampers. The hysteresis is then simplified into a trilinear model with elastic ($\mu_f < 1$), cracked ($\mu_c < \mu_f \leq 1$) and post-yield ($1 < \mu_f$) stages, where μ_f is the drift ductility at the target roof displacement (δ_{tar}) and μ_c the ratio of the crack-to-yield displacements, as depicted in Fig. 14 [23]. The secant stiffness ($K_{fu} = pK_f$) is further

related to the elastic lateral stiffness (K_f) by a stiffness ratio (p) given by Equation 5.a (cracked) or Equation 5.b (yielded), where α_1 is pre-yield stiffness ratio.

From the fitted trilinear pushover curve, the hysteretic energy (E_f) dissipated per cycle may then be calculated. The unloading stiffness of the RC members ($K_{ul} = (Q_{fc} + Q_f) / (\delta_{fc} + \mu_f \delta_{fy})$ for $\mu_c < \mu_f \leq 1$, or $K_{ul} = (Q_{fc} + Q_{fy}) / (\delta_{fc} + \delta_{fy}) / \mu_f^2$ for $1 < \mu_f$) is defined from the Takeda model, and reduces to Equation 6.a (cracked) or Equation 6.b (yielded), where the Takeda stiffness degradation parameter is taken as $\lambda = 0.4$ [55]. It should be noted that the unloading and reloading stiffness depend on the damage state, and evolutionary non-degrading rules have been proposed in previous studies [56–58], but are not included in the present study.

$$p = \frac{\mu_c + \alpha_1(\mu_f - \mu_c)}{\mu_f} \text{ for } (\mu_c < \mu_f \leq 1) \tag{5.a}$$

$$p = \frac{\mu_c + \alpha_1(1 - \mu_c)}{\mu_f} \text{ for } (1 < \mu_f) \tag{5.b}$$

$$E_f = 2pK_f(\mu_f \delta_{fy})^2 \cdot \frac{(1-p)\mu_c}{\mu_c + p\mu_f} \text{ for } (\mu_c < \mu_f \leq 1) \tag{6.a}$$

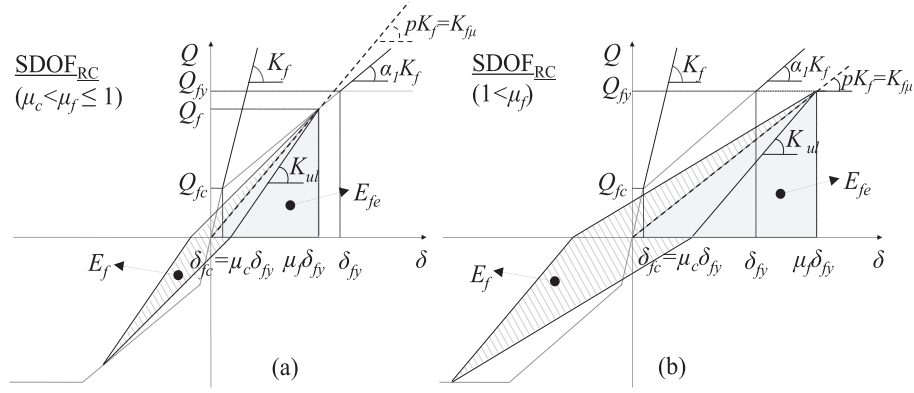


Fig. 14. SDOF_{RC} force-displacement hysteresis: (a) Cracked ($\mu_c < \mu_f \leq 1$) and (b) Yielding ($1 < \mu_f$) [23].

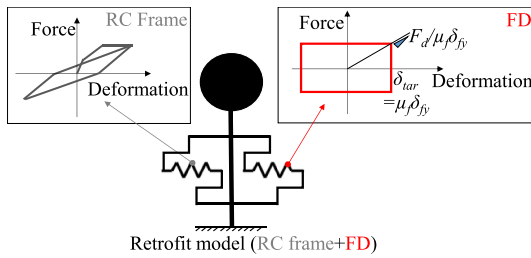


Fig. 15. Retrofitted SDOF model with FD.

$$E_f = 2pK_f(\mu_f\delta_{jy})^2 \frac{p\mu_f - p(1 + \mu_c)\mu_f^2 + \mu_c}{\mu_c + p\mu_f} \text{ for } (1 < \mu_f) \quad (6.b)$$

3.2. Friction damper sizing and vertical distribution

The friction brace dampers act in parallel with the existing RC moment frame (Fig. 15) to increase the lateral strength and provide a reliable source of energy dissipation. In this study, the elastic brace segment is designed to minimize the slip drift and exceeds the strength requirements imposed by the slip force. The independent selection of strength and stiffness is a key attribute that differs from BRBs, where the elastic segment is constrained by the restrainer dimensions and desire to maximize the yield length, resulting in closer relationship between the axial stiffness and yield force than friction dampers.

Furthermore, the experimental results from the previous section indicated that the selected friction material is well represented by a perfectly elasto-plastic hysteresis (Fig. 15). The present study recommends adding an inscribed steel frame (SF) to transfer the damper forces to the RC structure and help protect the existing RC members and connections. The steel frame acts partially-compositely with the existing RC frame and resists the additional forces imposed by the damper, an effect that has previously been studied experimentally [29] and numerically [46]. Note that the retrofitted bays are stacked vertically from the ground level to avoid increasing the axial demands on columns not enhanced by the steel frame. The beneficial effect of the damper and steel frame on the existing RC frame was addressed by reducing the required damper force in Section 3.3.

The required lateral force (F_d) of the friction dampers (referred to as

the “lateral slip force”) to achieve a target displacement (δ_{tar}) was extended from the stiffness-based CD method to incorporate the existing RC frame:

(a) First, the supplemental hysteretic energy dissipated per cycle by the friction damper (E_d) (Fig. 15) is given by Equation 7. Similarly, the strain energy is obtained from the combined secant stiffness at δ_{tar} .

$$E_d = 4F_d\delta_{tar} = 4F_d(\mu_f\delta_{jy}) \quad (7)$$

$$E_{\Sigma fe} = \frac{1}{2} \left(pK_f + \frac{F_d}{\mu_f\delta_{jy}} \right) (\mu_f\delta_{jy})^2 \quad (8)$$

(b) The equivalent damping (ξ'_{eq}) (Equation 9) was obtained from the total hysteretic energy ($E_f + E_d$) and total strain energy ($E_{\Sigma fe}$) (Equation (8)) in the peak cycle, and added to the estimated $\xi_{f0} = 0.03$ intrinsic damping of the existing RC frame [23].

$$\xi'_{eq} = \xi_{f0} + \frac{E_f + E_d}{4\pi E_{\Sigma fe}} \quad (9)$$

(c) As the displacement ductility in each cycle varies under earthquake ground motions, the effective equivalent damping [59] is lower than that at the peak cycle, and the saturated response reduction effect develops at a larger ductility than indicated by the peak cycle-ductility relationship. Nevertheless, previous studies [60] have shown that the more accurate average equivalent damping is about 0.6–0.8 of that calculated at the peak cycle. Other studies [23,27–28] have proposed a damping reduction factor of 0.6 for RC frames retrofitted with buckling-restrained braces, while the Japanese code [61] suggests 0.8 for seismic base isolation applications. Another study [62] investigated the application of friction dampers to steel frames, and found that a damping reduction factor of 0.7 best matched the numerical story drift results. The site class has also been noted to affect this factor [63], although 0.6–0.8 was achieved for 10%–20% peak-cycle equivalent damping. Therefore, a damping reduction factor (C_r) of 0.7 is adopted to simplify the equations, and is consistent with previous studies.

$$\xi_{eq} = \xi_{f0} + C_r \left(\frac{E_f + E_d}{4\pi E_{\Sigma fe}} \right) \quad (10)$$

(d) The supplemental hysteretic damping reduces the spectral demands by a damping response reduction factor (R). This study adopts an equation proposed by Kasai et al. [64] (Equation (11)) with the default calibration coefficient of $a = 25$, which was calibrated to the mean

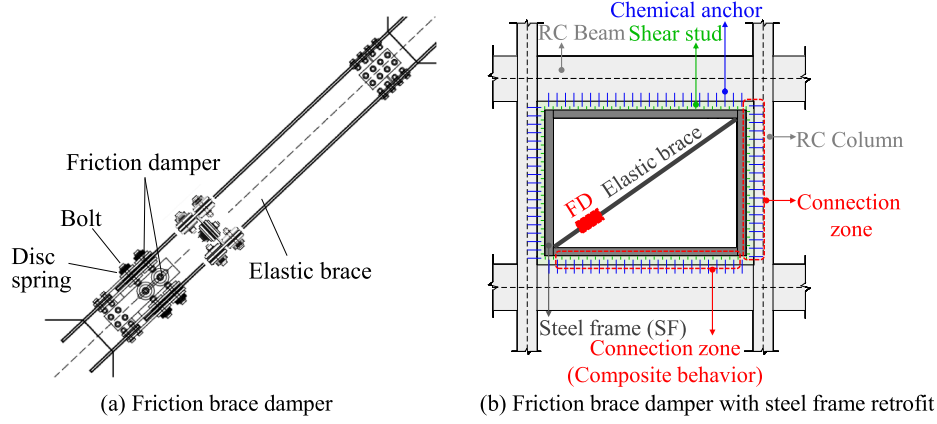


Fig. 16. Retrofit of RC frame using friction brace dampers with steel frames.

response of a suite of 31 earthquake ground motions. Note that $\xi_{f\mu}$ and ξ_{eq} are the averages of equivalent hysteretic damping of SDOF_{RC} and equivalent hysteretic damping of the retrofitted system, respectively.

$$R = \sqrt{\frac{1 + a \cdot \xi_{f\mu}}{1 + a \cdot \xi_{eq}}} \quad (11)$$

Therefore, the reduction to the target story drift (θ_{tar}) relative to the existing RC frame ($\theta_{f\mu}$) (Equation (12)) may be achieved from the product of R and the secant period ratio $T_{f\mu} / T_{\Sigma\mu}$, which is related to the secant stiffnesses of SDOF_{RC} (pK_f) and the retrofitted system ($pK_f + F_d / \delta_{tar}$). As the target displacement and ξ_{eq} are mutually dependent, Equation (12) is traditionally solved iteratively.

$$\begin{aligned} \frac{\theta_{tar}}{\theta_{f\mu}} &= \frac{T_{\Sigma\mu}}{T_{f\mu}} \sqrt{\frac{1 + a \cdot \xi_{f\mu}}{1 + a \cdot \xi_{eq}}} = \sqrt{\frac{pK_f}{pK_f + F_d / \delta_{tar}} \frac{1 + a \cdot \xi_{f\mu}}{1 + a \cdot \xi_{eq}}} \\ &= \sqrt{\frac{p}{p + F_d / (K_f \delta_{tar})} \frac{1 + a \cdot \xi_{f\mu}}{1 + a \cdot \xi_{eq}}} \quad (12) \end{aligned}$$

(e) Nevertheless, a closed-form solution may be obtained by solving for the normalized lateral slip force $f_d = F_d / (K_f \delta_{tar})$ given a target drift reduction $\theta_{tar} / \theta_{f\mu}$. This is achieved by substituting Equations (6)–(8) into Equation (10), and then into Equation (12), rearranging into constant, linear and higher order terms, and then solving the quadratic for f_d . For convenience, Equations 13.a and 13.b introduce two factors (A_{f1} , A_{f2}) that relate the cyclic hysteretic to strain energy of the RC frame, and reduce the final expression to Equations 14.a and 14.b for the cracked ($\mu_c < \mu_f \leq 1$) and yielding ($1 < \mu_f$) stages, respectively. As mentioned previously, λ is the unloading stiffness degradation parameter from the Takeda model and is taken as $\lambda = 0.4$ [55].

$$A_{f1} = \frac{(1-p) \cdot \mu_c}{\mu_c + p \mu_f} \text{ for } (\mu_c < \mu_f \leq 1) \quad (13.a)$$

$$A_{f2} = \frac{p \mu_f - p(1 + \mu_c) \mu_f^2 + \mu_c}{\mu_c + p \mu_f} \text{ for } (1 < \mu_f) \quad (13.b)$$

$$f_d = \frac{F_d}{K_f \delta_{tar}} = \frac{p \left(\left(\frac{\theta_{f\mu}}{\theta_{tar}} \right)^2 - 1 \right) \cdot \left(1 + a \left(\xi_{f0} + \frac{C_r A_{f1}}{\pi} \right) \right)}{1 + a \xi_{f0} + \frac{2a C_r}{\pi}} \text{ for } (\mu_c < \mu_f \leq 1) \quad (14.a)$$

$$f_d = \frac{F_d}{K_f \delta_{tar}} = \frac{p \left(\left(\frac{\theta_{f\mu}}{\theta_{tar}} \right)^2 - 1 \right) \cdot \left(1 + a \left(\xi_{f0} + \frac{C_r A_{f2}}{\pi} \right) \right)}{1 + a \xi_{f0} + \frac{2a C_r}{\pi}} \text{ for } (1 < \mu_f) \quad (14.b)$$

Equations 14.a and 14.b express the required normalized lateral slip force relative to the SDOF_{RC} system, and may be applied up the structure height by extending the CD method, which targets the same inelastic story drift ($\theta_{tar,i} = \theta_{tar}$) at each story.

(f). The required lateral slip force ($F_{d,i}$) at the i^{th} story is then derived by setting the same RC frame ductility (μ_f), post-yield stiffness factor (p) and normalized lateral slip force (f_d) at each story, and adopting a

vertical distribution of lateral forces (Q_i). The force distribution may be defined by the local design code, for example ASCE-SEI7 [51], which is adopted in this paper or the ‘‘Ai distribution’’ prescribed in the Japanese seismic provisions [65]. Given that the story drift is defined by each story’s shear force divided by the story stiffness and height, a constant maximum story drift (θ_{max}) may be assigned to every story and then set equal θ_{tar} . Applying these conditions, the local story drifts are related by Equation (15), which is an intermediate result also obtained in the original CD method [27,28]:

$$\theta_i = \frac{Q_i}{\left(K_{f\mu i} + \frac{F_{d,i}}{\delta_{tar,i}} \right) H_i} \times \frac{H_i}{H_i} = \frac{\sum_{i=1}^N (Q_i H_i)}{\sum_{i=1}^N \left[\left(K_{f\mu i} + \frac{F_{d,i}}{\delta_{tar,i}} \right) H_i^2 \right]} \frac{F_{d,i}}{\delta_{tar,i}} = \frac{f_d K_{f\mu i}}{p} \quad (15)$$

Rearranging Equation (15), $F_{d,i}$ is then expressed as Equation (16):

$$F_{d,i} = \frac{Q_i}{H_i} \frac{\sum_{i=1}^N (K_{f\mu i} H_i^2)}{\sum_{i=1}^N (Q_i H_i)} \left(1 + \frac{f_d}{p} \right) \delta_{tar,i} - K_{f\mu i} \delta_{tar,i} \quad (16)$$

Note that the story secant stiffness of the existing RC frame ($K_{f\mu,i}$) may be expanded using the post-yield stiffness factor (p) (Equation 5.a and 5.b) and story stiffness ($K_{f,i}$) at target lateral story displacement ($\delta_{tar,i}$), which equals $\theta_{tar} H_i$. A final closed-form solution for the required lateral slip force ($F_{d,i}$) at the i^{th} story is then given for the cracked ($\mu_c < \mu_f \leq 1$) and yielding ($1 < \mu_f$) stages by Equations 17.a and 17.b, as follows:

$$F_{d,i} = \frac{Q_i}{H_i} \frac{\sum_{i=1}^N (K_{f\mu i} H_i^2)}{\sum_{i=1}^N (Q_i H_i)} \left(1 + \frac{f_d \cdot \mu_f}{\alpha_1 (\mu_f - \mu_c) + \mu_c} \right) \delta_{tar,i} - K_{f\mu i} \delta_{tar,i} \text{ for } (\mu_c < \mu_f \leq 1) \quad (17.a)$$

$$F_{d,i} = \frac{Q_i}{H_i} \frac{\sum_{i=1}^N (K_{f\mu i} H_i^2)}{\sum_{i=1}^N (Q_i H_i)} \left(1 + \frac{f_d \cdot \mu_f}{\alpha_1 (1 - \mu_c) + \mu_c} \right) \delta_{tar,i} - K_{f\mu i} \delta_{tar,i} \text{ for } (1 < \mu_f) \quad (17.b)$$

3.3. Composite behavior between RC and retrofitted steel frames

The previous analysis is valid for friction brace dampers (Fig. 16a) directly connected to the existing RC beam-column joints (ignoring any damper-frame interaction effects). However, in practice, a supplemental steel frame internal to each bay is recommended to distribute the damper forces to the existing RC frame. As the primary purpose of the steel frame is to transmit axial forces and the continuous bracing provided by the grouted connection to the existing RC frame suppresses lateral torsional buckling, the steel members may be slender, contributing only a modest lateral stiffness ($K_{SF,i}$) when acting alone. Nevertheless, composite behavior between the new steel and existing RC

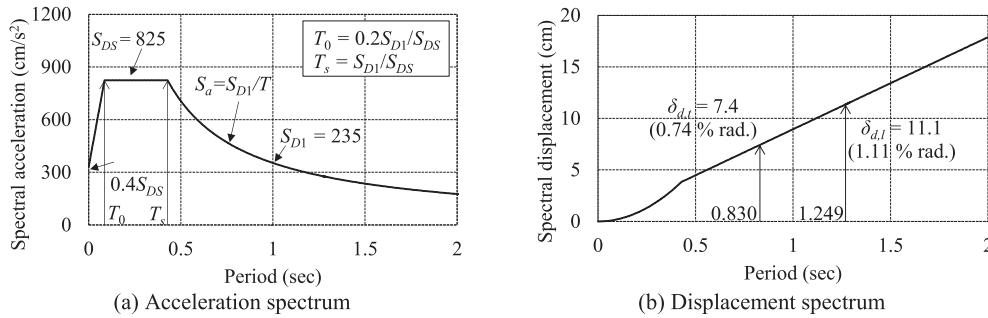


Fig. 17. MCE spectra for Chiang Rai, Thailand.

members may substantially enhance the stiffness of the existing RC frame; the stiffness of a single bay of which is denoted $K_{RC,i}$. A previous study by the authors [46] found that the grouted “connection zone” detail shown in Fig. 16b develops partially composite behavior at design level drifts. Furthermore, the amplification in stiffness for the actual partially composite behavior ($\gamma_{cp,i}$) at a single bay of the i^{th} story was found to be linearly related to the fully composite stiffness ratio ($\gamma_{cf,i}$), with both stiffness ratios taken with respect to the total non-composite component stiffness ($K_{RC,i} + K_{SF,i}$). Nonlinear pushover analysis for the example building suggested ratios of $\gamma_{cp,1} = 0.45 \gamma_{cf,1} + 0.55$ for the 1st story and $\gamma_{cp,i} = 0.25 \gamma_{cf,i} + 0.75$ for the upper stories, which also agreed with a single-story test specimen [29]. Note that $\gamma_{cp,i}$ and $\gamma_{cf,i}$ represent the composite behavior of a single bay and the increase relative to the story stiffness of the full RC frame ($K_{f,i}$) is much smaller.

As the steel frame sizes are determined by the damper slip forces at each story, which are not necessarily proportional to the RC frame, properly accounting for this effect would require a new pushover analysis whenever a steel frame is added or revised. However, incremental changes to the damper sizes produce diminishing returns, both in terms of the equivalent damping and seismic response. Furthermore, it is anticipated that the elastic forces developed by the partially composite steel frame will be small relative to the damper slip force. Therefore, it is proposed to simply reduce the required lateral slip force ($F_{dc,i}$) at the i^{th} story by the force developed by the partially composite steel frame at $\theta_{dy} = 1/1000$ rad, which is the slip drift adopted to design elastic segments in this study and is achievable in practice. Note that this implies that the friction dampers may be expected to slip under frequent serviceability level earthquakes, but the total number of slipping cycles over a 50 year design life are expected to be less than imposed in the experiment. Also, the selected material (C-1) exhibited a stable friction coefficient even under 100 continuous cycles (Fig. 4d), while the dampers are designed to prevent slipping under the ultimate wind force.

The reduction in required force due to composite behavior is further limited to no $>20\%F_{d,i}$, as this is the maximum reduction investigated in this study. Note that these are practical approximations used to rapidly arrive at a design solution, and it may be prudent to validate the final design, for example by directly including the steel frame in the pushover

analysis used to construct the SDOF model. Nevertheless, the proposed reduction to $F_{dc,i}$ is given by Equations (18.a) (1st story) and Equations 18.b (upper stories). When there is no SF and no composite behavior between RC and steel frame, $\gamma_{cp,1}$ and $\gamma_{cf,i}$ equal unity, and $F_{dc,i}$ converges to $F_{d,i}$.

$$F_{dc,1} = F_{d,1} - [K_{SF,1} + 0.45(\gamma_{cf,1} - 1)(K_{RC,1} + K_{SF,1})] \cdot (\theta_{dy} H_1) \geq 0.8F_{d,1} \quad (18.a)$$

$$F_{dc,i} = F_{d,i} - [K_{SF,i} + 0.25(\gamma_{cf,i} - 1)(K_{RC,i} + K_{SF,i})] \cdot (\theta_{dy} H_i) \geq 0.8F_{d,i} \text{ for } (i > 1) \quad (18.b)$$

3.4. Retrofit design steps

The step-by-step retrofit design method is summarized as follows:

1. Perform a nonlinear modal pushover analysis (based on the fundamental mode) and fit the roof displacement - base shear relationship to a trilinear backbone with elastic, cracked and yielding stages. Also obtain the story strengths of the existing RC frame ($Q_{fy,i}$).
2. Simplify the RC frame into a SDOF_{RC} model using Equations to, and calculate the energy dissipation (E_f) of the existing structure at the target drift (θ_{tar}) using Equations 5 to 6.
3. Obtain the maximum story drift of the existing RC frame from the SDOF_{RC} drift (θ_{fi}), noting that the existing frame may not be proportioned to achieve a uniform drift profile. If it exceeds the target story drift (θ_{tar}), then the building requires a seismic retrofit, while structures with maximum story drift less than θ_{tar} do not. The target story drift may be selected by the designer, but this study targeted 1/200 rad at MCE.
4. Calculate the required friction damper slip force ratio (f_d) from Equations 14.a or 14.b.
5. Vertically distribute the story damper slip forces ($F_{d,i}$) using Equation 17.a or 17.b.
6. (Optional) Size the steel frame to resist the axial forces generated by the friction damper. Slender steel sections may be used to maximize the steel frame’s yield drift, as lateral torsional buckling is

Table 3
Design results for the longitudinal direction.

| Story | Before retrofit | | Buckling-restrained brace (BRB) retrofit | | | | Friction damper (FD) retrofit | | |
|-------|----------------------|--------------------|--|----------------------------|---------------------|-------------------------|-------------------------------|-------------------|--------------------|
| | $K_{f,i}$ (kN/mm) | $Q_{fy,i}$ (kN) | Without steel frame | | With steel frame | | Without steel frame | With steel frame | |
| | | | $K_{BRB,i}$ (kN/mm) | $\delta_{BRB,y,i}$ (mm) | $F_{BRB,i}$ (kN) | $K_{BRBC,i}$ (kN/mm) | $F_{BRBC,i}$ (kN) | $F_{d,i}$ (kN) | $F_{dc,i}$ (kN) |
| | Pushover analysis | | [27,28] | | | [46] | | Equation 17.a | Equation 18 |
| 4th | 39.6 | 1228 | 16.8 | 4.8 | 81 | 6.5 | 31 | – | – |
| 3rd | 32.2 | 1127 | 100 | 5.3 | 531 | 74 | 393 | 395 | 361 |
| 2nd | 32.1 | 1124 | 145 | 5.3 | 767 | 119 | 630 | 609 | 575 |
| 1st | 45.3 | 1586 | 124 | 5.3 | 657 | 77 | 410 | 476 | 416 |

Table 4
Design results for the transverse direction.

| Story | Before retrofit | | Buckling-restrained brace (BRB) retrofit | | | | Friction damper (FD) retrofit | | |
|-------|----------------------|-------------------|--|---------------------------|---------------------|-------------------------|-------------------------------|-------------------|--------------------|
| | | | Without steel frame | | With steel frame | | Without steel frame | | With steel frame |
| | $K_{f,i}$ (kN/mm) | $Q_{y,i}$ (kN) | $K_{BRB,i}$ (kN/mm) | $\delta_{BRBy,i}$ (mm) | $F_{BRB,i}$ (kN) | $K_{BRBC,i}$ (kN/mm) | $F_{BRBC,i}$ (kN) | $F_{d,i}$ (kN) | $F_{dc,i}$ (kN) |
| | Pushover analysis | | [27,28] | | [46] | | Equation 17.a | | Equation 18 |
| 4th | 74.8 | 2319 | – | – | – | – | – | – | – |
| 3rd | 70.2 | 2457 | 79 | 5.3 | 415 | 60 | 317 | 308 | 274 |
| 2nd | 74.5 | 2608 | 131 | 5.3 | 688 | 103 | 539 | 613 | 578 |
| 1st | 106.6 | 3731 | 65 | 5.3 | 339 | 32 | 167 | 261 | 200 |

suppressed by the continuous bracing provided by the grouted connections to the RC frame.

- (Optional) Calculate $K_{SF,i}$ and $\gamma_{cf,b}$ and decrease the required story damper slip force to account for the partially composite steel frame using Equations 18.a and 18.b.

4. Validation of proposed retrofit method

4.1. Target building and seismic hazard

The proposed retrofit design method was applied to a four-story RC school building and validated using nonlinear response history analysis (NLRHA). The example building was located in Chiang Rai, the northernmost province of Thailand. Detailed frame dimensions and member sizes are provided in [46], while the minimum specified strengths for the 24 MPa concrete and 300 MPa rebar were adopted, with the seismic mass calculated as 184 tons for the 1st to 3rd stories and 171 tons for the 4th story. Three-dimension numerical models were built using ETABS [66], following the same modelling assumptions as described in a previous BRB retrofit study [46].

Modal analysis identified the first three periods as 1.249 sec (translation in the longitudinal direction), 0.871 sec (torsional deformation), and 0.830 sec (translation in the transverse direction), which are superimposed on the maximum considered event (MCE) acceleration and displacement spectra in Fig. 17a and 17b, respectively. The MCE spectrum was defined as 1.5 times the elastic, 5% damped design-level spectrum, which for Site Class D in Chiang Rai, Thailand [67] is defined by a short period spectral acceleration of $S_{DS} = 0.825$ g and 1 sec spectral acceleration of $S_{D1} = 0.235$ g.

A target story drift ratio (θ_{tar}) of 1/200 rad. (0.5% rad.) was selected to avoid damage to drift-sensitive nonstructural components, and increase the likelihood of achieving immediate occupancy after a strong earthquake. First, nonlinear pushover analysis was conducted for the four-story model of the existing RC frame, and the roof displacement-base shear relationship simplified into a trilinear backbone. The $SDOF_{RC}$ properties were then calculated as $H_{eq} = 10$ m (73.5% of building height), $M_{eq} = 577$ tons (80% of the total mass), $K_{fl} = 14.6$ kN/mm (lateral stiffness in the longitudinal direction) and $K_{ft} = 33.1$ kN/mm (lateral stiffness in the transverse direction). The MCE displacement spectrum (Fig. 17b) indicated $SDOF_{RC}$ displacements of $\delta_{d,l} = 111$ mm in the longitudinal direction and $\delta_{d,t} = 74$ mm in the transverse direction,

with corresponding maximum story drifts (SDR_{max}) of $\delta_{d,l} / H_{eq} = 1.11\%$ rad and $\delta_{d,t} / H_{eq} = 0.74\%$ rad. Both exceeded the target story drift, indicating that retrofit was required in both directions.

4.2. Retrofit design example

The friction brace dampers were then designed using the proposed retrofit design method, and compared to the existing RC building and a BRB retrofit scheme from the previous study [46]. The resulting friction damper and BRB sizes are shown in Table 3 (longitudinal direction) and Table 4 (transverse direction), along with the elastic story stiffnesses (K_f) of the existing RC frame obtained from the earlier pushover analysis. Note that the BRBs were designed using the conventional CD method [27,28] by specifying the required lateral stiffness ($K_{BRB,i}$), with the required lateral yield strength ($F_{BRB,i}$) obtained from the calculated yield deformation ($\delta_{BRBy,i}$). Note that a slightly smaller equivalent damping factor of $C_r = 0.6$ was found to better approximate the average equivalent damping for the BRB retrofit design [27,28], which led to slightly different retrofit requirements at the 4th story in the longitudinal direction than the friction damper retrofit. The reduced required stiffness ($K_{BRBC,i}$) and strength ($F_{BRBC,i}$) were also redesigned with supplemental steel frames, considering partial composite behavior [46].

The normalized lateral slip forces were calculated for the friction dampers using Equation 14.a as $f_d = 0.59$ in the longitudinal direction and $f_d = 0.18$ in the transverse direction, and the corresponding story slip forces ($F_{d,i}$) obtained from Equation 17.a. The required story slip forces ($F_{dc,i}$) were then reduced to account for the supplemental steel frames and partial composite behavior using Equation 18. No friction dampers were required to achieve the design target of $SDR_{tar} < 0.5\%$ rad at the 4th story in either direction. Also, the required damper force was lower for the friction dampers than for the BRBs. This was primarily attributed to the smaller yield drift of the friction brace dampers, which provided greater hysteretic energy dissipation at small drifts that the BRBs, with did not yield until about 0.3% drift. Although the equivalent damping of the two systems converged at larger drifts, friction dampers may be more effective for high performance retrofits of RC frames, which crack at relatively small drifts.

4.3. Design of friction brace dampers

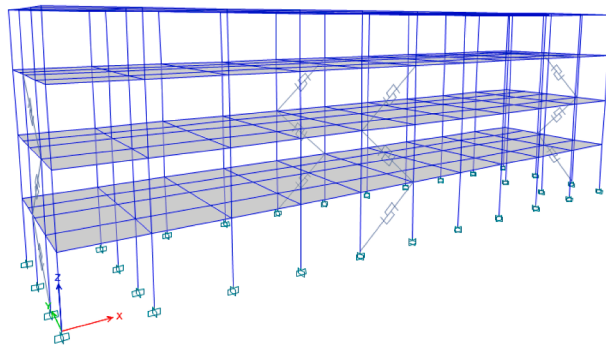
Each friction brace damper consisted of a friction damper and elastic

Table 5
Friction brace damper design in longitudinal direction.

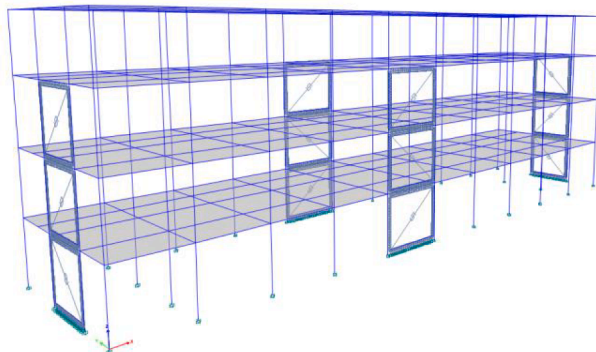
| Story | H_i (mm) | L_i (mm) | Dampers # | $\sigma F_{d,i}$ (kN) | Elastic segment | $\rho K_{d,i}$ (kN/mm) | $\rho \delta_{dy,i}$ (mm) | $\delta_{dy,i}$ (mm) | $\theta_{dy,i}$ (rad) |
|-------|---------------|---------------|--------------|--------------------------|-----------------|---------------------------|------------------------------|-------------------------|--------------------------|
| 4th | 3100 | 4000 | – | – | – | – | – | – | – |
| 3rd | 3500 | 4000 | 2 | 263 | SHS 150x150x9x9 | 183 | 1.43 | 1.91 | 1/1837 |
| 2nd | 3500 | 4000 | 2 | 405 | SHS 150x150x9x9 | 183 | 2.21 | 2.94 | 1/1192 |
| 1st | 3500 | 4000 | 2 | 316 | SHS 150x150x9x9 | 183 | 1.73 | 2.29 | 1/1526 |

Table 6
Friction brace damper design in transverse direction.

| Story | H_i (mm) | L_i (mm) | Dampers # | $\rho F_{d,i}$ (kN) | Elastic segment | $\rho K_{d,i}$ (kN/mm) | $\rho \delta_{dy,i}$ (mm) | $\delta_{dy,i}$ (mm) | $\theta_{dy,i}$ (rad) |
|-------|---------------|---------------|--------------|------------------------|-----------------|---------------------------|------------------------------|-------------------------|--------------------------|
| 4th | 3100 | 3500 | – | – | – | – | – | – | – |
| 3rd | 3500 | 3500 | 2 | 218 | SHS 150x150x9x9 | 197 | 1.20 | 1.70 | 1/2064 |
| 2nd | 3500 | 3500 | 2 | 433 | SHS 150x150x9x9 | 197 | 2.17 | 3.06 | 1/1143 |
| 1st | 3500 | 3500 | 2 | 185 | SHS 150x150x9x9 | 197 | 0.77 | 1.09 | 1/3218 |



(a) Without steel frame (3D-RF)



(b) With partially composite steel frame (3D-RSCF)

Fig. 18. 3-D view of the analysis models.

Table 7
Definition of numerical models.

| Model name | Description |
|---------------|--|
| 3D-R model | Existing RC building (Bare RC) |
| 3D-RB model | RC building retrofitted with BRBs (BRB Retrofit) |
| 3D-RF model | RC building retrofitted with friction brace dampers (FD Retrofit) |
| 3D-RSCB model | RC building retrofitted with BRBs and steel frame, including composite behavior (BRB + SF Retrofit including composite behavior) |
| 3D-RSCF model | RC building retrofitted with friction brace dampers and steel frames, including composite behavior (FD + SF Retrofit including composite behavior) |

segments, and was intended to start slipping at a story drift ($\theta_{dy,i}$) of less than 1/1000 rad, which increases the damper efficiency and justifies the assumed elasto-perfectly plastic hysteresis. The elastic segment was also designed to not buckle from the axial force generated by the friction damper. Given the maximum required lateral slip force of 613 kN from Table 4, two dampers each with an axial slip force of $\rho F_{d,i} = 433$ kN were

selected with 150 × 9 mm square hollow section (SHS) elastic segments. The axial workpoint stiffness ($\rho K_{d,i}$) and slip deformation ($\rho \delta_{dy,i}$) are listed in Tables 5 and 6 per damper at each story, along with the corresponding lateral yield displacements and drift angles.

4.4. Numerical model

Five 3D models were then constructed to validate the seismic performance of the retrofit designs. The existing RC building model was denoted 3D-R and used as a benchmark. This model and the BRB retrofit models with (3D-RSCB) and without (3D-RB) supplemental steel frames were previously presented in [46]. Friction brace damper retrofits were modelled without a supplemental steel frame (3D-RF) and are shown in Fig. 18a. Each friction brace damper was modeled as a link element using a Wen model [66,68], with the axial workpoint stiffness (due to the elastic segment) assigned to the linear “effective stiffness” and nonlinear “stiffness” in ETABs, and the required slip force as the nonlinear “yield strength”. Next, supplemental steel frames with partial composite behavior were modelled (3D-RSCF) using the same MLP link approach adopted in [46], as depicted in Fig. 18b. The five models are summarized in Table 7.

4.5. Elastic modal properties

Fig. 19a and Fig. 20a show the first three translation modes in the longitudinal and transverse directions, indicating that the fundamental periods decreased after adding the BRBs and friction brace dampers. Substituting some of the required damper force with steel frames only had a minor effect on the fundamental period. Furthermore, the fundamental mode shapes only slightly changed in the retrofitted models, becoming more linear in Fig. 19b and Fig. 20b.

4.6. Nonlinear response history analysis

Nonlinear response history analysis (NLRHA) was performed for all five models using a suite of eleven scaled ground motions, and the average and average plus one standard deviation of the maximum story responses were tabulated for each model. Note that only the first horizontal ground motion component was applied, once in the longitudinal and once in the transverse direction. This enabled a direct comparison of the performance about the two building axes, but slightly underestimated the interstory drift at the corners.

4.6.1. Ground motions for NLRHA

The ground motions (GM) were selected from the PEER NGA West 2 database [69] based on the local source fault characteristics, which were similar for both the design and maximum considered hazard. Scale factors between 0.68 and 1.89 were applied to the selected records [46] for the design basic earthquake (DBE) suite, and then further scaled by 1.5 for the maximum considered earthquake (MCE) suite following ASCE 7-16 [51] (Fig. 21).

4.6.2. Maximum story drift ratio

The maximum interstory drift ratios (SDR_{max}) at each story in the two orthogonal directions are shown in Fig. 22a to 22f (longitudinal

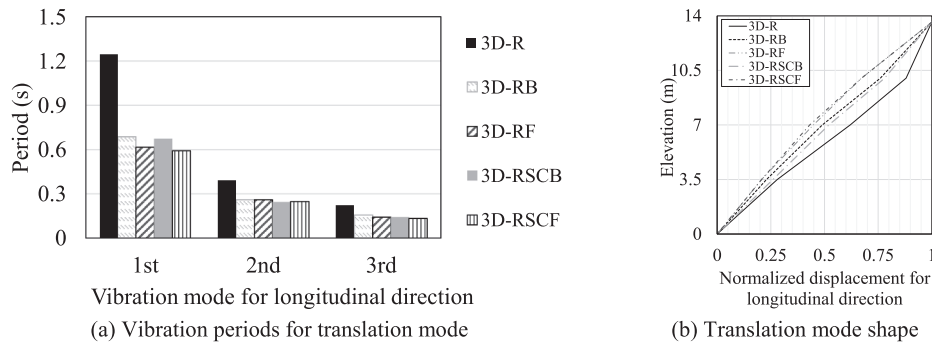


Fig. 19. Modal analysis results for the longitudinal direction.

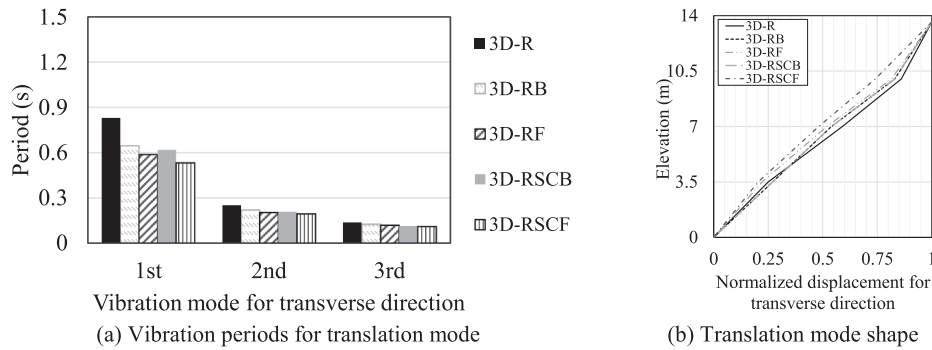


Fig. 20. Modal analysis results for the transverse direction.

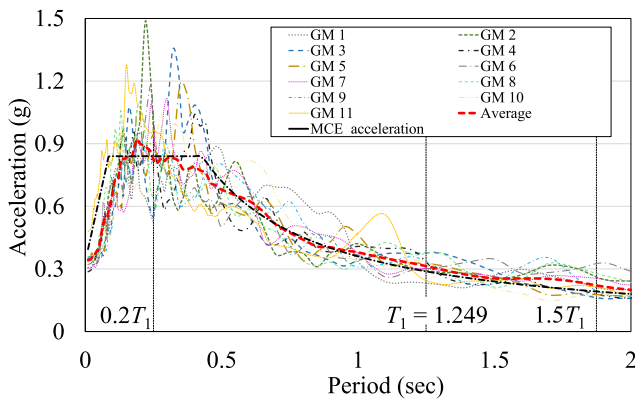


Fig. 21. Target MCE and scaled ground motion elastic response spectra (5% damped).

direction) and Fig. 23a to 23f (transverse direction). Fig. 22a and 23a depict the drift profiles for the existing RC building model (3D-R), indicating that the average SDR_{max} significantly exceeded the target of 0.5% rad in the 1st–3rd stories, while the 4th story drift was marginal in the longitudinal direction and clearly already acceptable in the transverse direction. Furthermore, Fig. 22c and 23c confirm that the friction brace damper retrofit (3D-RF) was able to limit the average SDR_{max} to <0.5% rad in both directions at all stories, even without supplemental steel frames. The retrofit was also successful in suppressing the drift concentration observed at the 2nd story in the existing RC building. Incorporating supplemental steel frames with partial composite behavior and a corresponding reduction in friction damper size (3D-RSCF) produced nearly identical results, with Fig. 22e and 23e once again achieving an average SDR_{max} < 0.5%. The performance of the friction brace damper retrofit was comparable to the previous BRB

retrofit designs, which are shown in Fig. 22b and 23b (3D-RB) and Fig. 22d and 23d (3D-RSCB). The near-identical average drift responses with and without supplemental steel frames (Fig. 22f and 23f) confirm the effectiveness of using the elastic steel frames to reduce the required friction damper slip forces, similar to how supplemental steel frames reduced the required BRB stiffness [46].

4.6.3. Residual story drift ratio

The residual inter-story drift ratios (SDR_{re}) were obtained at the end of an additional 60 sec of free vibration, as residual drift may significantly influence the usability of a building following a strong earthquake. The average and average plus one standard deviation SDR_{re} are shown in Fig. 24 for longitudinal direction, while the transverse direction exhibited similar trends. Each of the retrofitted models achieved SDR_{re} < 0.1%, implying that an immediate occupancy performance level is feasible, even in a large earthquake.

4.6.4. Maximum roof acceleration

The maximum roof accelerations (A_{max}) are shown in Fig. 25a (longitudinal direction) and Fig. 25b (transverse direction) for each ground motion, and the average of these results are shown in Fig. 26a (longitudinal direction) and Fig. 26b (transverse direction). Although the increased stiffness of the retrofitted buildings will tend to increase the roof floor accelerations due to the period shift, depending on the spectral shape of the ground motion, this is offset by the increased hysteretic damping attributed to the hysteretic energy dissipated by the dampers. Nevertheless, the net effect was minimal for this design example, but should be confirmed after retrofitting a building with dampers if nonstructural damage to acceleration-sensitive components is of concern.

While brittle failure modes of the existing RC members were not directly considered in this analysis, the recommended steel frame (3D-RSCB and 3D-RSCF) helped distribute the damper forces to the existing RC members. Furthermore, the partially composite steel frame

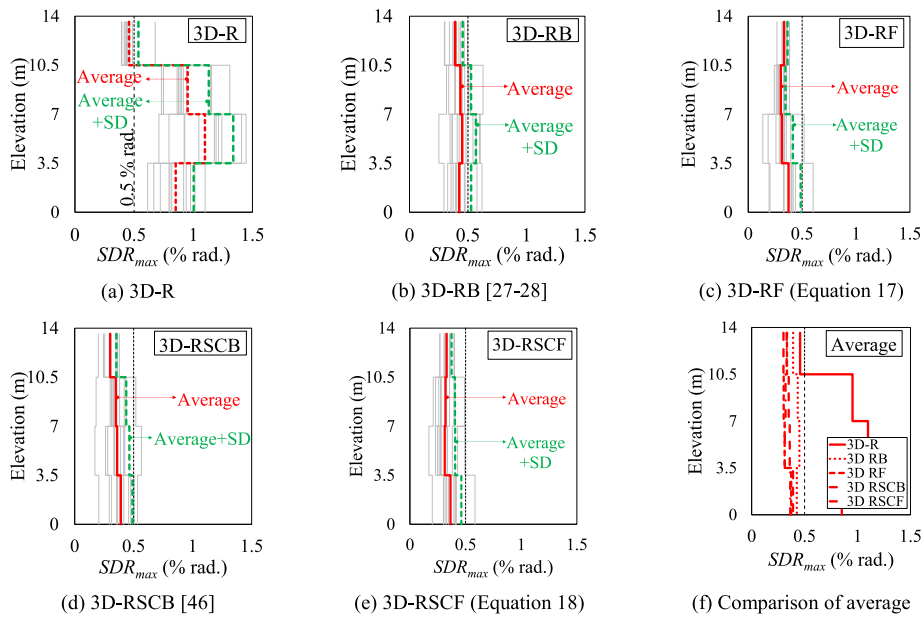


Fig. 22. Maximum story drift ratio for the longitudinal direction.

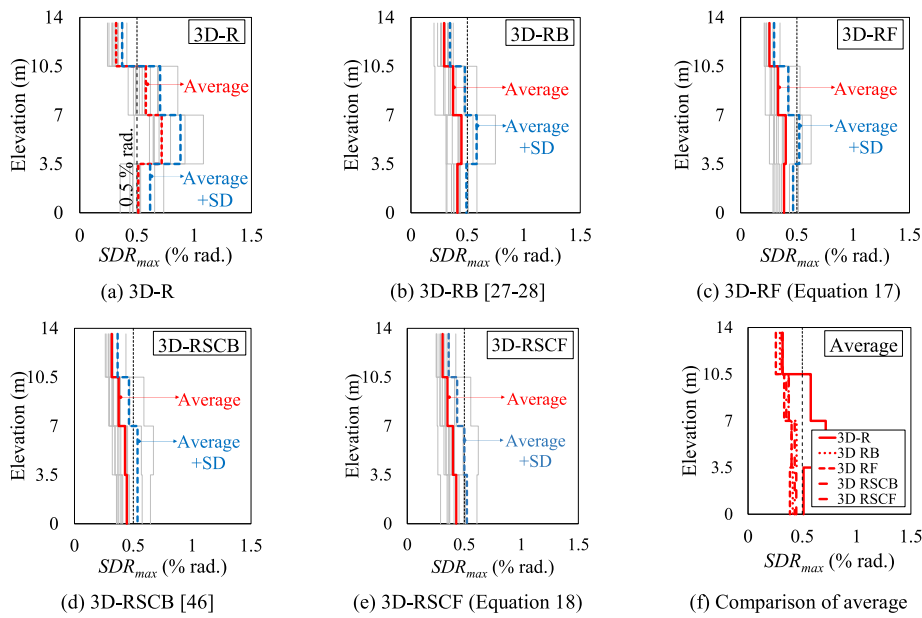


Fig. 23. Maximum story drift ratio for the transverse direction.

strengthens the directly connected RC members and the improved story drift reduces the flexural demands on the unconnected members. Therefore, the proposed retrofit scheme reduces demands on the existing RC members. Nevertheless, practical applications should consider the project-specific RC member strengths, and the inclusion of dampers does not preclude the need to retrofit deficient members.

5. Conclusions

This study experimentally characterized the dynamic friction coefficient of five candidate friction brace damper materials, and a material with a high, stable friction coefficient and negligible friction dependencies was selected. Next, a seismic design method based on equivalent linearization was proposed for RC moment frames retrofitted

with friction brace dampers. Based on the experimental and analytical results, the following conclusions may be drawn:

- 1) The first two friction materials with polymer composite compositions (A-1 and A-2) exhibited relatively stable rigid-plastic slip behavior, but the average friction coefficient decreased with increasing temperature and the first cycles at room temperature varied by $\pm 10\%$. A polymer composite material B was sensitive to the maximum slip velocity, as well as temperature.
- 2) Two sintered metal friction materials were tested and found to produce stable friction coefficients with negligible amplitude, velocity and temperature dependencies. The sintered metal material C-1 was selected as it achieved highly stable, near-constant friction

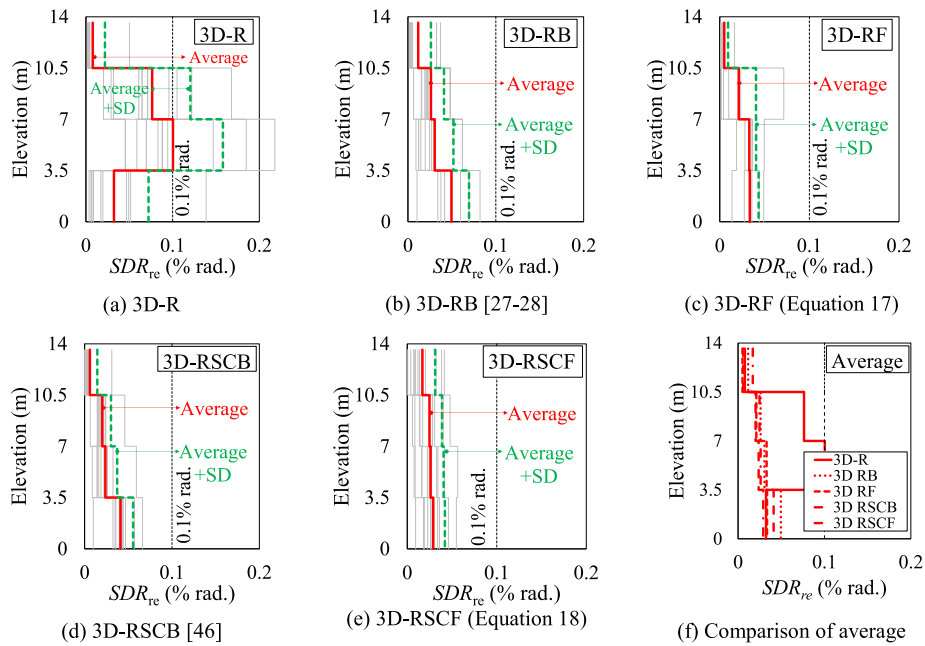


Fig. 24. Residual story drift ratio for the longitudinal direction.

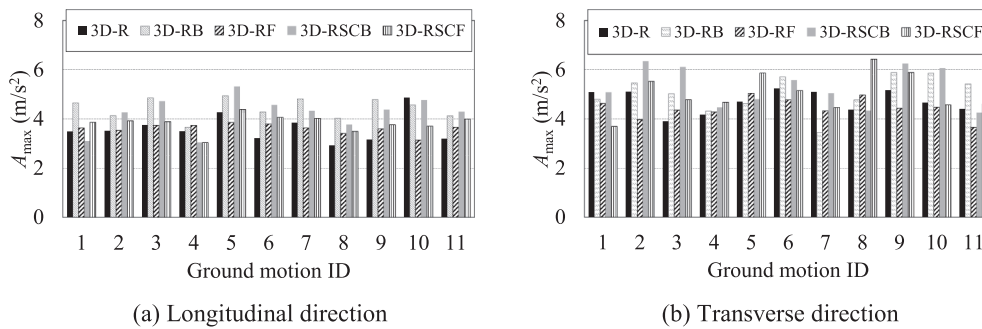


Fig. 25. Maximum roof acceleration.

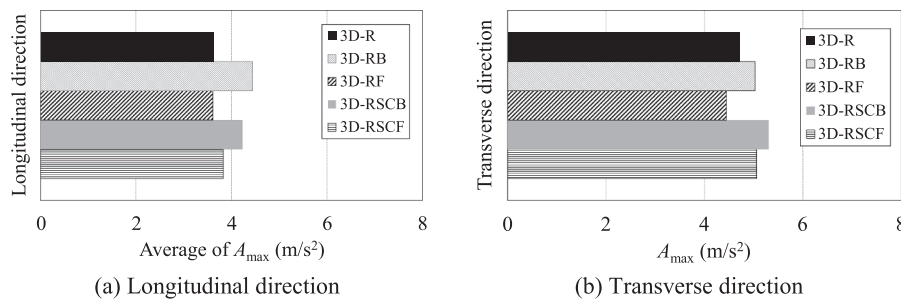


Fig. 26. Average of maximum roof acceleration.

coefficient of $\bar{\mu} = 0.40$, permitting an elasto-perfectly plastic hysteresis for modelling and design purposes.

- 3) A closed-form retrofit design method was derived to directly determine the required slip force, including with supplemental steel frames exhibiting partial composite behavior with the existing RC frame. The NLRHA results confirmed that the proposed retrofit method was able to limit the average of the maximum interstory drifts to less than the target 0.5%. Furthermore, the peak drift was nearly identical for retrofits employing friction brace dampers designed using the proposed method and BRBs designed using the

conventional CD method, and with or without supplemental steel frames, confirming the efficacy of the proposed method.

- 4) An example four story RC moment frame was retrofitted with the selected friction brace dampers using the proposed method. NLRHA indicated that the peak and residual inter-story drifts were substantially improved after retrofitting the existing RC building with friction brace dampers, while roof accelerations were not critical. This implies that both structural and nonstructural damage may be effectively mitigated using the proposed retrofit design strategy, increasing the likelihood of immediate occupancy after a major earthquake.

CRedit authorship contribution statement

Panumas Saingam: Conceptualization, Methodology, Investigation, Formal analysis, Writing - original draft. **Ryota Matsuzaki:** Validation, Investigation, Visualization. **Koki Nishikawa:** Validation, Investigation, Visualization. **Ben Sittler:** Investigation, Visualization, Writing - review & editing. **Yuki Terazawa:** Validation, Investigation, Visualization. **Toru Takeuchi:** Supervision, Project administration, Conceptualization, Writing - review & editing.

Declaration of Competing Interest

The authors declare that they have no known competing financial interests or personal relationships that could have appeared to influence the work reported in this paper.

Acknowledgement

The authors are grateful to T. Yoshikawa, S. Kudo, M. Unno from Showa Denko Materials Co.Ltd., K. Minowa, A. Watanabe from Nippon Steel Engineering Co., Ltd., and Dr. Ryota Matsui from Hokkaido University for collaborating on the friction experiments and insightful discussions.

References

- Mitchell D, DeVall RH, Saatcioglu M, Simpson R, Tinawi R, Tremblay R. Damage to concrete structures due to the 1994 Northridge earthquake. *Can J Civ Eng* 1995;22(2):361–77.
- Mitchell D, DeVall RH, Kobayashi K, Tinawi R, Tso WK. Damage to concrete structures due to the January 17, 1995, Hyogo-ken Nanbu (Kobe) earthquake. *Can J Civ Eng* 1996;23(3):757–70.
- Tsai KC, Hwang SJ. Seismic Retrofit Program for Taiwan School Buildings After FTER 1999 Chi-Chi Earthquake. 14th World Conference on Earthquake Engineering; 2008.
- Lukkunaprasit P, Ruangrassamee A, Boonyatee T, Chintanapakdee C, Jankaew K, Thanasisathit N, et al. Performance of Structures in the Mw 6.1 Mae Lao Earthquake in Thailand on May 5 2014 and Implications for Future Construction. *J Earthquake Eng* 2016;20(2):219–42.
- Celik OC. Holistic Seismic Behavior and Design of Buildings. *FACADE Conf* 2017: 161–73.
- Masi A, Chiauzzi L, Santarsiero G, Manfredi V, Biondi S, Spacone E, et al. Central Italy earthquake the Amatrice case study. *Bull Earthq Eng* 2019;17(10):5631–54.
- Binici B, Ozecebe G, Ozelik R. Analysis and design of FRP composites for seismic retrofit of infill walls in reinforced concrete frames. *Composite: Part B* 2007;38(5-6):575–83.
- Ozcan O, Binici B, Ozecebe G. Improving seismic performance of deficient reinforced concrete columns using carbon fiber-reinforced polymers. *Eng Struct* 2008;30(6):1632–46.
- Foutch DA, Hjeltnad KD, Calderón EDV, Gutiérrez EF, Downs RE. The Mexico earthquake of September 19, 1985: Case studies of seismic strengthening for two buildings in Mexico City. *Earthq Spectra* 1989;5(1):153–74.
- Canbay E, Ersoy U, Ozecebe G. Contribution of reinforced concrete infills to seismic behavior of structural systems. *ACI Struct J* 2003;100:637–43.
- Badoux M, Jirsa JO. Steel bracing of RC frames for seismic retrofitting. *J Struct Eng* 1990;116(1):55–74.
- Fukuyama H, Sugano S. Japanese seismic rehabilitation of concrete buildings after the Hyogoken-Nanbu earthquake. *Cem Concr Compos* 2000;22(1):59–79.
- Jara M, Hernández C, García R, Robles F. The Mexico earthquake of September 19, 1985: Typical cases of repair and strengthening of concrete buildings. *Earthq Spectra* 1989;5(1):175–93.
- Jirsa JO. Divergent issues in rehabilitation of existing buildings. *Earthq Spectra* 1994;10:95–112.
- Pall AS, Marsh C. Response of friction damped braced frames. *J Struct Eng* 1982; 108:1313–23.
- Aiken I, Kelly S. Earthquake simulator testing and analytical studies of two energy absorbing systems for multi-storey structures. Report No. UCB/EERC-90/03, EERC, Berkeley; 1990.
- Fitzgerald TF, Anagnos T, Goodson M, Zsutty T. Slotted bolted connections in a seismic design of concentrically braced connections. *Earthq Spectra*, EERI 1989;5(2):383–91.
- Grigorian CE, Popov EP. Slotted bolted connection energy dissipaters. *Earthq Spectra* 1993;9(3):491–504.
- Nims DK, Richter PJ, Bachman RE. The use of the energy dissipation restraint for seismic hazard mitigation. *Earthq Spectra* 1993;9(3):467–87.
- Chandra J, Warnitchai P. Application of Buckling Restrained Braces for Seismic Strengthening of Irregular Gravity Load Designed Reinforced Concrete Frame Buildings. *Civil Eng Dimen* 2011;13:65–74.
- Di Sarno L, Manfredi G. Experimental tests on full-scale RC unreinforced frame and retrofitted with buckling-restrained braces. *Earthquake Eng Struct Dyn* 2012;41(2): 315–33.
- Habibi A, Chan RWK, Albermani F. Energy-based design method for seismic retrofitting with passive energy dissipation systems. *Eng Struct* 2013;46:77–86.
- Sutcu F, Takeuchi T, Matsui R. Seismic Retrofitting Design Method of Existing RC Buildings with Buckling Restrained Braces. *J Constr Steel Res* 2014;101:304–13.
- Khampanit A, Leelataviwat S, Kochanin J, Warnitchai P. Energy-based seismic strengthening design of non-ductile reinforced concrete frames using buckling-restrained braces. *Eng Struct* 2014;81:110–22.
- Mahrenholtz C, Lin P-C, Wu A-C, Tsai K-C, Hwang S-J, Lin R-Y, et al. Retrofit of reinforced concrete frames with buckling-restrained braces. *Earthq Eng Struct Dyn* 2015;44(1):59–78.
- Almeida A, Ferreira R, Proença JM, Gago AS. Seismic retrofit of RC building structures with Buckling Restrained Braces. *Eng Struct* 2017;130:14–22.
- Fujishita K, Sutcu F, Matsui R, Takeuchi T. Damage distribution based energy-dissipation retrofit method for multi-story RC building in Turkey. *IABSE Symposium Report* 2015;104:1–8.
- Takeuchi T, Wada A. Buckling-restrained braces and application. The Japan Society of Seismic Isolation.
- Sutcu F, Bal A, Fujishita K, Matsui R, Celik OC, Takeuchi T. Experimental and Analytical Studies of Sub-Standard RC Frames Retrofitted with Buckling-Restrained Braces and Steel Frames. *Bull Earthq Eng* 2020;18(5):2389–410.
- López-Almansa F, de la Cruz ST, Taylor C. Experimental study of friction dissipaters for seismic protection of building structures. *Earthq Eng Vib* 2011; 10(4):475–86.
- Santos AF, Santiago A, Rizzano G. Experimental response of friction dampers under different loading rates. *Int J Impact Eng* 2019;132:103316. <https://doi.org/10.1016/j.ijimpeng.2019.103316>.
- Qu Z, Ji X, Shi X, Wang Y, Liu H. Cyclic loading test of steel coupling beams with mid-span friction dampers and RC slabs. *Eng Struct* 2020;203:109876. <https://doi.org/10.1016/j.engstruct.2019.109876>.
- Xu YL, Ng CL. Seismic Protection of a Building Complex Using Variable Friction Damper: Experimental Investigation. *Eng Mech* 2008;134(8):637–49.
- Imad H, Mualla IH, Belev B. Performance of steel frames with a new friction damper device under earthquake excitation. *Eng Struct* 2002;24:365–71.
- Khoo H-H, Clifton C, Butterworth J, MacRae G. Experimental Study of Full-Scale Self-Centering Sliding Hinge Joint Connections with Friction Ring Springs. *J Earthq Eng* 2013;17(7):972–97.
- Khoo H-H, Clifton C, Butterworth J, MacRae G, Gledhill S, Sidwell G. Development of the self-centering Sliding Hinge Joint with friction ring springs. *J Constr Steel Res* 2012;78:201–11.
- Ramhormozian S, Clifton GC, MacRae GA, Davet GP. Stiffness-based approach for Belleville springs use in friction sliding structural connections. *J Constr Steel Res* 2017;138:340–56.
- Priestley MJN. Displacement-Based Seismic Assessment of Reinforced Concrete Buildings. *J Earthq Eng* 1997;1(1):157–92.
- Chopra AK, Goel RK. Direct Displacement-Based Design: Use of Inelastic vs. Elastic Design Spectra. *Earthq Spectra* 2001;17:47–64.
- Lin YY, Tsai MH, Hwang JS, Chang KC. Direct displacement-based design for building with passive energy dissipation systems. *Eng Struct* 2003;25(1):25–37.
- Maley TJ, Sullivan TJ, Corte GD. Development of a Displacement-Based Design Method for Steel Dual Systems With BucklingRestrained Braces and Moment-Resisting Frames. *J Earthq Eng* 2010;14(sup1):106–40.
- Mazza F, Vulcano A. Displacement-based design procedure of damped braces for the seismic retrofitting of r.c. framed buildings. *Bull Earthq Eng* 2015;13(7): 2121–43.
- Mazza F. A simplified retrofitting method based on seismic damage of a SDOF system equivalent to a damped braced building. *Eng Struct* 2019;200:109712. <https://doi.org/10.1016/j.engstruct.2019.109712>.
- Mazza F. Displacement-based seismic design of hysteretic damped braces for retrofitting in-plan irregular r.c. framed structures. *Soil Dyn Earthq Eng* 2014;66: 231–40.
- Kasai K, Fu Y, Watanabe A. Passive Control Systems for Seismic Damage Mitigation. *J Struct Eng ASCE* 1998;124(5):501–12.
- Saingam P, Sutcu F, Terazawa Y, Fujishita K, Lin P-C, Celik OC, et al. Celik O.C and Takeuchi T Composite Behavior in RC Buildings Retrofitted using Buckling-Restrained Braces with Elastic Steel Frames. *Eng Struct* 2020;219:110896. <https://doi.org/10.1016/j.engstruct.2020.110896>.
- Chanchi Golondrino JC, MacRae GA, Chase JG, Rodgers GW, Clifton GC. Behaviour of asymmetrical friction connections using different shim materials. New Zealand Society for Earthquake Engineering (NZSEE) Annual Conference; 2012. Paper Number 100.
- Sano T, Suzui Y, Hino Y, Takahashi Y. Development of Friction Slip Damper using High Tension Bolts, Report of Obayashi Corporation Technical Research Institute 2001; 62: 13-20, 2001 (in Japanese).
- Sano T, Nomura J. Development of Friction Slip Damper using High Tension Bolts (Part2), Report of Obayashi Corporation Technical Research Institute 2006; 70: 1-6 (in Japanese).
- Shirai K, Sano T, Suzui Y, Kageyama M, Kikuchi M. Development of Friction Damper with Displacement Dependent Variable Damping Force Characteristics. *AIJ J Technol Des* 2012;18(38):85–90 (in Japanese).
- American Society of Civil Engineers (ASCE). Minimum Design Loads for Buildings and Other Structures 2016 (ASCE/SEI 7-16).
- Chopra A. K. Dynamics of Structures: Theory and Applications to Earthquake Engineering, 5th ed.

- [53] Shibata A. Dynamics Analysis of Earthquake Resistant Structures. Tohoku University Press: Sendai.
- [54] Kuramoto H, Masaomi Teshigawara M, Okuzoto T, Koshika N, Takayama M, and Hori T. Predicting the earthquake response of buildings using equivalent single degree of freedom system. 12th World Conference on Earthquake Engineering 2000; Paper No. 1039.
- [55] Takeda T, Sozen MA, Nielsen NN. Reinforced concrete response to simulated earthquakes. *J Struct Eng ASCE* 1970;12(96):2557–73.
- [56] Wen Y-K. Method for random vibration of hysteretic systems. *J Eng Mech Div ASCE* 1976;102(2):249–63.
- [57] Song J-K, Pincheira JoséA. Spectral displacement demands of stiffness-and strength-degrading systems. *Earthq Spectra* 2000;16(4):817–51.
- [58] Mazza F. A plastic-damage hysteretic model to reproduce strength stiffness degradation. *Bull Earthq Eng* 2019;17(6):3517–44.
- [59] Newmark N, Rosenblueth B. *Fundamentals of earthquake engineering*. Prentice Hall; 1971.
- [60] Lin YY, Chang KC. Study on Damping Reduction Factor for Buildings under Earthquake Ground Motions. *J Struct Eng ASCE* 2003;129(2):206–14.
- [61] Ministerial Notification No. 2009 of the Ministry of Construction, Japan; 2000 (in Japanese).
- [62] Matsuzaki R. Mechanical characteristics and passive control effectiveness of friction dampers with various friction materials. Master thesis, Tokyo Institute of Technology; 2020.
- [63] Lin Y-Y, Chang K-C. Effects of Site Classes on Damping Reduction Factors. *J Struct Eng ASCE* 2004;130(11):1667–75.
- [64] Kasai K, Ito H, Watanabe A. Peak response prediction rule for a SDOF elasto plastic system based on equivalent linearization technique. *J Struct Constr Eng (Trans AIJ)* 2003;68(571):53–62.
- [65] The Building Center of Japan. The Building Standard Law of Japan on CD-ROM 2016.
- [66] Wilson EL. *CSI Analysis Reference Manual For SAP 2000, ETABS, SAFE, and CSI Bridge*. Berkeley: Computers & Structures, Inc; 2015.
- [67] Department of Public Works and Town & Country Planning (DPT), Thailand Seismic Design Code 2009.
- [68] Quaketek, Seismic Design with Friction Dampers. <https://www.quaketek.com/seismic-design/>.
- [69] Pacific Earthquake Engineering Research Center (PEER). PEER NGA Ground Motion Database, <https://ngawest2.berkeley.edu/site>.